



**HAL**  
open science

## Melilite-bearing lavas in Mayotte (France): An insight into the mantle source below the Comores

Anne-Aziliz Pelleter, Martial Caroff, Carole Cordier, Patrick Bachèlery, Pierre Nehlig, Delphine Debeuf, Nicolas Arnaud

► **To cite this version:**

Anne-Aziliz Pelleter, Martial Caroff, Carole Cordier, Patrick Bachèlery, Pierre Nehlig, et al.. Melilite-bearing lavas in Mayotte (France): An insight into the mantle source below the Comores. *Lithos*, 2014, 208-209, pp.281-297. 10.1016/j.lithos.2014.09.012 . insu-01089376

**HAL Id: insu-01089376**

**<https://insu.hal.science/insu-01089376v1>**

Submitted on 5 Dec 2014

**HAL** is a multi-disciplinary open access archive for the deposit and dissemination of scientific research documents, whether they are published or not. The documents may come from teaching and research institutions in France or abroad, or from public or private research centers.

L'archive ouverte pluridisciplinaire **HAL**, est destinée au dépôt et à la diffusion de documents scientifiques de niveau recherche, publiés ou non, émanant des établissements d'enseignement et de recherche français ou étrangers, des laboratoires publics ou privés.

1 Melilite-bearing lavas in Mayotte (France): an insight into the mantle  
2 source below the Comores

3  
4 Anne-Aziliz Pelleter <sup>a,1</sup>, Martial Caroff <sup>a,\*</sup>, Carole Cordier <sup>b,c</sup>, Patrick Bachelery <sup>d</sup>, Pierre  
5 Nehlig <sup>e</sup>, Delphine Debeuf <sup>f</sup>, Nicolas Arnaud <sup>g</sup>

6  
7 <sup>a</sup>UMR CNRS n°6538 « Domaines Océaniques », Institut Universitaire Européen de la Mer,  
8 Université de Brest, 6 avenue Victor Le Gorgeu, CS 93837, F-29238 Brest Cédex 3, France

9 <sup>b</sup>Université Grenoble Alpes, ISTERre, F-38000 Grenoble, France

10 <sup>c</sup> CNRS, ISTERre, F-38041 Grenoble, France

11 <sup>d</sup>Laboratoire Magmas et Volcans, UMR n°6524 CNRS-IRD-Université Blaise Pascal,  
12 Observatoire de Physique du Globe de Clermont-Ferrand, 5, rue Kessler, F-63038 Clermont-  
13 Ferrand Cédex, France

14 <sup>e</sup> Bureau de Recherches Géologiques et Minières, 3, avenue Claude-Guillemin, BP 36009, F-  
15 45060 Orléans Cédex 2, France

16 <sup>f</sup> Laboratoire GéoSciences Réunion, Faculté des Sciences et Technologies, 15, avenue René  
17 Cassin, CS 92003, F-97744 Saint-Denis Cédex 9, La Réunion, France

18 <sup>g</sup> Géosciences Montpellier, UMR 5243, CC 60, Université Montpellier 2, Place E. Bataillon,  
19 F-34095 Montpellier Cédex 5, France

20  
21 \* Corresponding author: caroff@univ-brest.fr

22 <sup>1</sup> Present address : UMR CNRS n°7327, Institut des Sciences de la Terre d'Orléans,  
23 Université d'Orléans, 1A rue de la Férolierie, 45071 Orléans, France (anne-  
24 aziliz.pelleter@univ-orleans.fr)

25

26 Keywords: Comores; ocean island basalts; olivine melilitite; HIMU; mantle heterogeneity;  
27 metasomatism

28

## 29 **1. Introduction**

30

31 Olivine melilitites are alkaline and ultracalcic basic igneous rocks rich in melilite, a  
32 calcic sorosilicate, and devoid of feldspar. They are thought to be produced by low degree of  
33 partial melting of a CO<sub>2</sub>-rich mantle source in both continental and oceanic contexts  
34 (Gudfinnsson and Presnall, 2005; Dasgupta et al., 2007). In continental zones, they are found  
35 at or near rifting zones, often in association with carbonatites. In the African continent,  
36 (olivine) melilitites have been observed in Sahara (Dautria et al., 1992), East African Rift  
37 (Bailey et al., 2005; Dawson, 2012; Mattsson et al., 2013), South Africa (Rogers et al., 1992;  
38 Janney et al., 2002), and Madagascar (Melluso et al., 2011). In oceanic setting, the olivine  
39 melilitites are produced in intraplate volcanoes (Maaløe et al., 1992; Hoernle and Schmincke,  
40 1993). They correspond generally to post-erosional, late units (Brey, 1978). In the vicinity of  
41 the Africa continent, olivine melilitites have been collected in Gran Canaria (Brey, 1978;  
42 Hoernle and Schmincke, 1993) and Cape Verde Islands (Brey, 1978). Several authors have  
43 highlighted the chemical resemblance, for incompatible trace element and isotopic ratios,  
44 between (olivine) melilitites and ocean island basalts (OIB), sometimes with a HIMU (or high  
45  $\mu$ , where  $\mu = {}^{238}\text{U}/{}^{204}\text{Pb}$ ) affinity (Rogers et al., 1992; Wilson et al., 1995; Janney et al., 2002).

46 The Comores Archipelago, composed of four volcanic islands (Mayotte, Anjouan,  
47 Moheli, and Grande Comore) is located in the Mozambique Channel between the continental  
48 blocks of Africa and Madagascar (Fig. 1). The initial volcanism period of the oldest island –  
49 Mayotte – onto the ocean floor is estimated to be ca. 15-10 Ma (Nougier et al., 1986), whereas  
50 the Karthala volcano of Grande Comore (the youngest island) is still active.

51           The mantle beneath the Comores is probably metasomatized, with modal amphibole  
52 and/or phlogopite (Späth et al., 1996; Class and Goldstein, 1997). In fact, Coltorti et al.  
53 (1999) evidenced a CO<sub>2</sub>-related cryptic metasomatism episode beneath Grande Comore. The  
54 origin of the Comores volcanism is attributed by Hajash and Armstrong (1972) and Emerick  
55 and Duncan (1982) to the upwelling of a mantle plume. Nougier et al. (1986) proposed that  
56 the Comorian magmas derive from the upper mantle, beneath an ocean-continent transitional  
57 crust structured by old and deep lithospheric fractures, which were reactivated during late  
58 Tertiary. Four Comores lavas – one sample from Moheli and the three analyzed samples from  
59 Anjouan (Reisberg et al., 1993; Späth et al., 1996; Salters and White, 1998) – have a more  
60 radiogenic Pb composition than the other Indian OIB. They display an isotopic signature close  
61 to that of the Atlantic islands near the western African coast, as Cape Verde and Canary  
62 Islands (Sushchevskaya et al., 2013).

63           The present study of Mayotte Island (Comores Archipelago), based on new  
64 petrological and geochemical data, reveals the coexistence of a large number of melilite-  
65 bearing (including olivine melilitites) and HIMU-like lavas (with  $^{206}\text{Pb}/^{204}\text{Pb} > 20$ ). Mayotte  
66 Island is thus a good example for studying the genesis of melilite-bearing lavas and their  
67 relation with a specific mantle composition.

68

## 69 **2. Geological setting**

70

71           Mayotte is the oldest island of the Comores archipelago (Fig. 1), emplaced, while  
72 intraplate, in an active tectonic area. The present-day geography of the area is the  
73 consequence of the Permian-Trias Karoo NW-SE rifting, which resulted in the separation  
74 between Gondwana and Indian-Madagascan continental blocks (Malod et al., 1991; Piqué,  
75 1999). The oceanic basins of Somalia and Mozambique opened during the Jurassic, while the

76 Madagascar Island drifted southwards along the Davie Ridge. The main part of the  
77 sedimentary products in the Mozambique Channel results from the erosion of the Davie Ridge  
78 resurrected during an Eocene compression phase (Leclaire et al., 1989). Since the middle  
79 Miocene, the tectonic regime in the Mozambique Channel is dominated by E-NE–W-SW  
80 extension, also identified in the East African Rift and in Madagascar (Bertil and Regnault,  
81 1998; Piqué, 1999).

82         Although the volcano morphology in the Comores archipelago is rather consistent  
83 with a chronological progression of the volcanism northwestwards (freshest reliefs in Grande  
84 Comore; presence of a coral reef only in Mayotte and, to a less extend, in Moheli: Fig. 1), the  
85 K-Ar geochronological data of the archipelago suggest a more complex history (Fig. 1). With  
86 exception of Grande Comore, in which old lavas do not crop out, each island displays a  
87 Neogene volcanic activity (shield stage?) together with a more recent one. The oldest  
88 subaerial lavas of the archipelago are found in Mayotte, consistently with its eroded  
89 morphology and the presence of a large coral reef. Only one coarse-grained rock of Anjouan  
90 is older ( $11.1 \pm 0.5$  Ma, Nougier et al., 1986), very different from the shield lavas (from  
91  $3.9 \pm 0.3$  Ma to  $1.5 \pm 0.2$  Ma, Nougier et al., 1986). However, no dating is available for the  
92 rocks constituting the submarine flanks of the islands. It is therefore very difficult to  
93 reasonably establish, or not, a chronological progression of volcanism throughout the  
94 archipelago.

95         Mayotte is located 300 km westward of Madagascar and 70 km southwestward of  
96 Anjouan (Fig. 1). It is constituted of two main volcanic islands (Grande Terre and Petite  
97 Terre:  $348 \text{ km}^2$  and  $16 \text{ km}^2$  in surface, respectively) and around twenty islets, within a lagoon  
98 of  $1100 \text{ km}^2$  bordered by a 160 km-long coral reef (Fig. 2a). Grande Terre is a north-south  
99 lengthened island, culminating at 660 m (Bénara Mount). The emerged reliefs correspond to  
100 the superstructure of two coalescent eroded shield volcanoes, subsiding for 1.5 Ma (Debeuf,

101 2004; Nehlig et al., 2013). Petite Terre is a 5 km-long island located 4 km eastward of Grande  
102 Terre (Fig. 2d).

103

### 104 **3. Sampling and analytical techniques**

105

#### 106 *3.1. Sampling*

107

108 The rocks presented here were collected during three field trips, in 2001 (sampling: D.  
109 Debeuf and P. Bachelery), 2010 and 2011 (sampling: P. Nehlig, F. Lacquement, and J.  
110 Bernard, with the financial and logistic support of the French BRGM).

111 Mayotte Island is characterized by an intense lateritic weathering and an important  
112 plant cover. Consequently, the main part of the volcanic substratum cannot be sampled.  
113 Although only the freshest rocks have been collected, a residual meteoric alteration induces  
114 relatively high loss on ignition (LOI) values in several samples. As all the samples having a  
115 LOI > 4.6 wt.% are affected by significant argillaceous / hydroxidic alteration, we have  
116 rejected them for the geochemical study.

117 Among about a hundred of samples collected in 2001, 24 lavas have been dated; 51  
118 samples have been analyzed for major and trace elements, 17 for  $^{87}\text{Sr}/^{86}\text{Sr}$ , 23 for  $^{143}\text{Nd}/^{144}\text{Nd}$   
119 isotopes, and 8 for Pb isotopes. Among the 35 samples collected in 2010 and 2011: 19  
120 samples have been analyzed for major and trace elements, 10 for  $^{87}\text{Sr}/^{86}\text{Sr}$  isotopes, and 14 for  
121 Nd and Pb isotopes. A selection of geochronological and chemical data is shown in Tables 1,  
122 2, and 3. The complete dataset is given in the supplementary Table S1.

123

#### 124 *3.2. $^{40}\text{Ar}/^{39}\text{Ar}$ datations*

125

126 Bulk rock samples (flows, dykes and domes) were dated by the  $^{40}\text{Ar}/^{39}\text{Ar}$  method.  
127 Analyses were performed on the 150- 250  $\mu\text{m}$ -size groundmass fraction. For each sample, one  
128 or more aliquots on different separates (typically feldspar and volcanic glass) were irradiated  
129 on January 2002 at the McMaster reactor, Ontario, in the 5C position for 26 h under a  $10^{18}$   
130 neutrons  $\text{cm}^{-2}\text{s}^{-1}$  flux. The irradiation standard is a Fish Canyon sanidine standard with an age  
131 of  $28.02 \pm 0.16$  Ma (Renne et al., 1998), with reproductive values within 0.6%.

132 Ages were obtained at the University of Montpellier 2, following a protocol similar to  
133 that described in Arnaud et al. (2003) and Garcia et al. (2003). Details on the analytical  
134 conditions are available from the authors upon request. Age given from age spectra are  
135 weighted mean plateaus (Fleck et al., 1977) or simple mean ages. The latter case corresponds  
136 to the situation where either subsequent steps overlap only at the  $1\sigma$  level or total  $^{39}\text{Ar}$   
137 cumulated from these steps is insufficient to define a classical plateau. All errors from age  
138 spectra take the error on the J factor into account. Plateau criterions being rarely achieved,  
139 sometimes simple mean age is given. The isochron ages are obtained in an inverse isochron  
140 diagram of  $^{36}\text{Ar}/^{40}\text{Ar}$  versus  $^{39}\text{Ar}/^{40}\text{Ar}$  (Roddick et al., 1980), which allows homogeneous  
141 excess components to be individualized in many occasions. Errors on age and intercept age  
142 include individual errors on each point and linear regression by York's method (York, 1969).  
143 The goodness of it relative to individual errors is measured by Mean Square Weighted  
144 Deviation (MSWD).

145

### 146 *3.3. Mineral and whole rock analyses*

147

148 Mineral compositions have been determined using a Cameca SX-100 electron  
149 microprobe (Microsonde Ouest, Brest, France) with an acceleration voltage of 15 kV and a  
150 beam current of 20 nA. Some high precision analyses of olivine were acquired using a JEOL

151 JXA-8230 electron microprobe (ISTerre, Grenoble, France) with an acceleration voltage of 25  
152 kV and a beam current of 900 nA.

153 Major and trace element analyses for the rocks sampled in 2001 were determined at  
154 the CRPG (Centre de Recherches Pétrographiques et Géochimiques, Nancy, France), whereas  
155 samples collected in 2010-2011 were analyzed at the PSO/IUEM (Pôle Spectrométrie Océan,  
156 Institut Universitaire Européen de la Mer, Brest, France). Whole-rock major elements were  
157 analyzed by inductively coupled plasma atomic emission spectrometry (ICP-AES) following  
158 the analytical method described by Cotten et al. (1995). Relative standard deviations are < 2%  
159 (< 1% for SiO<sub>2</sub>). Whole-rock trace elements were analyzed by inductively coupled plasma  
160 mass spectrometry (ICP-MS) following the sample preparation and analysis method of Barrat  
161 et al. (1996). Relative standard deviations are < 5% for most of the trace elements and < 10%  
162 for Nb, Gd, Tb, Ta, Ni, Zn and Rb. The concentrations found in the Mayotte OIB are well  
163 above the detection limits for all the trace elements analyzed.

164 Sr and some Nd isotopic ratios were measured by thermal ionization mass  
165 spectrometry (TIMS, Laboratoire Magmas et Volcans, Clermont-Ferrand, France and  
166 PSO/IUEM/IFREMER, Brest, France), while Pb and some Nd isotopic ratios were measured  
167 on a multicollector ICP-MS (PSO/IFREMER, Brest, France). Samples were leached in 2N  
168 HCl for about one hour and rinsed three times in ultrapure water to remove weathering effect.  
169 The protocol for element separation is described in Chauvel et al. (2011). Measured blanks  
170 are lower than 20 picograms (pg) for Nd, 60 pg for Sr and 100 pg for Pb (except one analysis  
171 session with 300 pg blank). Values used for mass fractionation corrections and relative  
172 standard deviations are given in Table 3.

173

#### 174 **4. Geochronology of Mayotte**

175



176 Four volcanic domains have been recognized on Mayotte Island from geological and  
177 geomorphological observations, ages available in the literature (Hajash and Armstrong, 1972;  
178 Emerick and Duncan, 1982; Nougier et al, 1986; McDougall unpublished in Debeuf, 2004),  
179 and new  $^{40}\text{Ar}/^{39}\text{Ar}$  ages obtained on 24 samples (Table 1).

180 The most eroded – and thus oldest – area is the southern part of the main island (Fig.  
181 2b), where the hydrographic network is intensely erosive and most headlands correspond to  
182 inverted reliefs. The main building volcanic phase (> 10.6--~3.0 Ma) is mainly formed by  
183 alkali basalt, basanite and olivine nephelinite lava flows (Fig. 2c), strongly weathered to  
184 lateritic products. This phase ended with the intrusion of around fifteen phonolitic protrusions,  
185 associated with nephelinitic/phonolitic lava flows and pyroclastic density currents (3.9-3.1  
186 Ma). The post-shield phase began with the emplacement of the tephriphonolitic/phonolitic  
187 Combani massif circa 2.4 Ma ago. The last events in the south domain are emission of  
188 pyroxene-bearing basanitic and nephelinitic lava flows (ca. 2.0--~1.5 Ma).

189 The northwest domain is characterized by sharp reliefs of moderately weathered  
190 basaltic-basanitic lava flow piles, contemporaneous to the southern main building phase (>  
191 7.1--~4.0 Ma). These lavas constitute a second shield volcano, which would have emerged  
192 after the southern one (Stieljes, 1988). Lavas are cut by a basaltic intrusive network (sills and  
193 N–S-trending dykes). This volcanism was followed by an extension-related mafic  
194 magmatism, at about ~4.0-< 1.0 Ma, which renewed the reliefs. The two melilititic lava flows  
195 were probably emplaced during this event. Phonolitic domes (3.3 and 2.5 Ma) are especially  
196 rare (Fig. 2c).

197 The north central sector of Grande Terre is characterized by the least eroded, youngest  
198 reliefs (Fig. 2b). This is consistent with lava ages mainly comprised between 2.4 and 0.8 Ma,  
199 i.e. more recent than in both south and northwest domains. Two older samples have been  
200 dated at 3.4 Ma (Hajash and Armstrong, 1972) and 3.35 Ma (Emerick and Duncan, 1982), but

201 they have not been analyzed for major and trace elements. From west to east, the north central  
202 sector is composed of: (1) the Digo massif, made of basaltic-tephritic lava flows; and (2) the  
203 Mtsapéré stratovolcano (basaltic-tephritic lava flows intruded by phonolitic protrusions, Fig.  
204 2c), lying on the northwest shield formations.

205         The fourth volcanic zone is a recent explosive complex comprising small pyroclastic  
206 edifices (tuff rings and cones) built by phreatomagmatism and strombolian eruptions along  
207 the east coast of Grande Terre and in Petite Terre (Fig. 2c). The activity is estimated from  
208 500 000 to 150 000 years in Grande Terre and up to 4 000 years in Petite Terre, where the  
209 volcanic edifices lay on a Holocene barrier reef younger than 9000 years (Camoin et al.,  
210 2004). The subaerial explosive volcanoes lay on lateritized lava flows in Grande Terre. The  
211 first strombolian phase built edifices with interbedded lava flows and pyroclastic levels  
212 (scoriaceous blocks and lapilli, and ash). Then, the volcanism became phreatoplinian, with  
213 pumice-bearing tuff ring structures. Two of them crop out in Grande Terre and four in Petite  
214 Terre (three in the eastern part and a fourth in the southernmost area, Fig. 2c).

215

## 216 **5. Petrology**

217

### 218 *5.1. Lavas and hypabyssal rocks*

219

220         The mineral assemblage of the studied lavas is presented in Fig. 3. The petrographic  
221 nomenclature is based on mineralogy, total alkali-silica (TAS) and basanite-nephelinite-  
222 melilitite classification schemes of Le Bas et al. (1986) and Le Bas (1989), respectively (Figs.  
223 4 and 5).

224         Most of the lava flows of south and northwest domains are alkali basalts and basanites.  
225 Lavas are usually porphyritic, sometimes cumulative (> 35 vol.% phenocrysts), with

226 clinopyroxene and/or olivine (Fo<sub>79-85</sub>) phenocrysts. Groundmass generally has a microlitic  
227 texture. It is constituted of clinopyroxene (fassaite-diopside), olivine (Fo<sub>62-81</sub>), plagioclase  
228 (An<sub>47-64</sub>), nepheline, Fe-Ti oxides and apatite. Perovskite crystals have been identified as  
229 inclusions in clinopyroxene phenocrysts of one basanite from the south domain.

230 Two olivine melilitite lavas were collected near Mtsangamouji in the northwest  
231 domain. They are porphyritic with zoned olivine phenocrysts (Fo<sub>84-88</sub>) immersed in a  
232 microlitic groundmass constituted of melilite, olivine (Fo<sub>79-84</sub>), titanomagnetite, apatite,  
233 clinopyroxene, and tiny nepheline. One sample displays mingling features.

234 Olivine-free and olivine-bearing nephelinites occur as lava flows or dykes in the south  
235 domain and in a few areas of the northwest domain. They have a porphyritic texture with  
236 phenocrysts of clinopyroxene (fassaite-diopside) and nepheline. Groundmass crystals include  
237 nepheline, clinopyroxene, Fe-Ti oxides, and apatite. Olivine phenocrysts (Fo<sub>74-87</sub>) and  
238 microcrysts (Fo<sub>69-78</sub>) are only present in the olivine nephelinites, whereas hornblende,  
239 aegirine-augite, perovskite and titanite are detected only in olivine-free nephelinites.  
240 Microcrystals of melilite (< 10 vol.%) have been identified in two olivine nephelinites (PN2  
241 and PN12f).

242 Tephritic and tephriphonolitic lavas occur in the south and north central domains.  
243 They have a porphyric fluidal microlitic texture. Phenocrysts are zoned augite and kaersutite,  
244 whereas groundmass includes plagioclase, clinopyroxene, Fe-Ti oxides, hastingsite and  
245 apatite. Tephriphonolites can be distinguished from tephrites by the presence of both K-  
246 feldspar as phenocrysts and arfvedsonite and aegirine-augite as microcrysts.

247 Phonolites occur as protusions or as derived lava flows, mainly in the south and north  
248 central domains and, sparsely, in the northwest one. They have a porphyritic microlitic  
249 texture, sometimes fluidal. Diopside, hornblende, K-feldspar, nepheline, and apatite occur as

250 phenocrysts and microcrysts. Moreover, the groundmass contains titanite, aegirine-augite,  
251 ferro-arfvedsonite, ferro-eckermannite and Fe-Ti oxides.

252

## 253 *5.2. Pyroclastites and cumulates*

254

255 Two types of pyroclastic formations have been identified: strombolian and  
256 phreatoplinian deposits, mainly located in the most recent domains of Mayotte (NE coast of  
257 Grande Terre and Petite Terre), and only sparsely represented in the older north central and  
258 south domains (Fig. 2c). Elements of the primary pyroclastic breccias are locally reworked as  
259 volcanogenic sedimentary deposits.

260 The strombolian edifices are small reddened scoria cones, composed of basaltic  
261 indurated lapilli- and bomb-sized fragments alternating with lava flows and ash levels.  
262 Locally, blocks of sedimentary rock (sandstone, arkose) are embedded in the breccias. The  
263 fragments bear iddingsitized olivine, pyroxene, nepheline and Fe-Ti oxides.

264 The phreatoplinian deposits are constituted of meter-sized interbedded sequences of  
265 pumice levels and hyaloclastite layers. Pumices range in size from 5 to 50 cm. They have a  
266 vesicular hyaloporphyric texture, with euhedral phenocrysts of K-feldspar, hornblende, and  
267 Fe-Ti oxides. Among the xenoliths, fragments of coral, lavas and scoria, dunitic and  
268 pyroxenitic cumulates are present. The basanitic xenolith PN5b, cumulative in olivine and  
269 clinopyroxene, has been found in the pumice sample PN5a.

270 Cumulates have been collected as xenoliths or blocks. They are dunites, pyroxenites,  
271 essexites and ijolites.

272

## 273 **6. Geochemistry**

274

275 *6.1. Major elements*

276

277         The subsequent geochemical study focuses on lavas and hypabyssal rocks (dykes and  
278 protrusions) of Grande Terre, together with pumices of Petite Terre. Major and trace element  
279 compositions of representative samples from Mayotte are listed in Table 2. The TAS diagram  
280 of Le Bas et al. (1986) (Fig. 4) can be used to evidence a large alkaline association in Mayotte  
281 from alkali basalts (only four analyzed samples), basanites and foidites to phonolites through  
282 intermediate lavas. Two trends are observed (Fig. 4): the first one, including mainly the south  
283 lavas, one basalt apart (M41), is highly silica-undersaturated; the second one, including the  
284 rocks from the three other domains, is moderately silica-undersaturated. Mafic rocks ( $\text{MgO} >$   
285  $5 \text{ wt.}\%$ ) are divided into three groups on the basis of silica-undersaturation, alkalinity and  
286 calcium content: basalts/basanites, olivine nephelinites and olivine melilitites (Fig. 5). Most of  
287 the nephelinites and olivine melilitites are gathered in the foidite field in the TAS diagram  
288 (Fig. 4). In general, silica-undersaturation increases from north central lavas to south shield  
289 lavas through northwest shield lavas (Fig. 4). Eleven olivine nephelinites and the two olivine  
290 melilitites contain CIPW normative larnite ( $n_{\text{larnite}}$ :  $\text{Ca}_2\text{SiO}_4$ ), with contents higher than 10  
291 % normative for olivine melilitites (Fig. 5), consistently with the criterion proposed by  
292 Wooley et al. (1996) to define this type of lavas. According to Médard et al. (2004), olivine  
293 melilitites can be considered as ultracalcic lavas ( $\text{CaO} > 13.5 \text{ wt.}\%$  and  $\text{CaO}/\text{Al}_2\text{O}_3 > 1 \text{ wt.}\%$ ).

294         Plots of  $\text{CaO}$ ,  $\text{Al}_2\text{O}_3$ ,  $\text{K}_2\text{O}$ , and  $\text{P}_2\text{O}_5$  against  $\text{MgO}$  are shown in figure 6.  $\text{CaO}$  is  
295 positively correlated with  $\text{MgO}$  for lavas with  $\text{MgO} < 8 \text{ wt.}\%$ . The  $n_{\text{larnite}}$  samples and the  
296 mafic xenolith PN5b of Petite Terre have the highest  $\text{CaO}$  contents ( $> 12 \text{ wt.}\%$ ). The  
297 (tephri)phonolites of the Combani massif form a low- $\text{CaO}$  trend together with the lavas of the  
298 north central zone.  $\text{Al}_2\text{O}_3$  and  $\text{K}_2\text{O}$  display remarkable negative correlations with  $\text{MgO}$ .

299 Except for the  $P_2O_5$ -rich N-larnite-bearing lavas,  $P_2O_5$  increases with decreasing MgO up to  
300 MgO ~ 5 wt.%, then decreases.

301

## 302 *6.2. Trace elements*

303

304 We investigate in Figs. 6e-h the chemical distinction of the volcanic domains using  
305 incompatible trace element variations against Th.

306 (1) The post-shield lavas of the north central domain form linear trends versus Th.

307 They are distributed in two groups with different Th concentrations and variable contents on  
308 Nb, Hf, and Yb. These samples have the lowest Nb/Zr ratios of the collection, displaying a  
309 decreasing trend with increasing Th.

310 (2) The recent phonolitic pumices of Petite Terre have the highest Nb, Hf, and Yb  
311 contents. Their Nb/Zr values range from 0.25 to 0.27.

312 (3) Most of the south domain samples plot linearly on the trace variation diagrams.  
313 Most of the corresponding lavas are contemporaneous with the shield phase. The trend has a  
314 slope especially low in the Hf versus Th diagram of figure 6f. The south domain samples are  
315 scattered in the Nb/Zr versus Th diagram of figure 6h.

316 (4) Amongst the south domain samples, the figure 6 diagrams can be used to  
317 discriminate four lavas, all of them located in the post-shield Combani massif. They plot apart  
318 in both Nb and Hf vs. Th diagrams (Fig. 6e and f), together with the Petite Terre pumices,.

319 (5) The northwest domain, mainly constituted of shield mafic lavas, cannot be easily  
320 distinguished in the figure 6 trace diagrams. The corresponding lavas plot either in the north  
321 central trend (Fig. 6a and f) or with the southern samples (Fig. 6e and g). Post-shield olivine  
322 melilitites M66 and FL386, presented above, belong to this domain.

323 Mafic samples (alkali basalts, basanites, olivine nephelinites and olivine melilitites)  
324 from Mayotte are enriched in light and middle REE (LREE and MREE, respectively) with  
325 respect to heavy REE (HREE), consistently with their OIB characteristics (Fig. 7a). Slope of  
326 the REE patterns increases from basalts/basanites to olivine nephelinites and to olivine  
327 melilitites. These latter are also slightly more enriched in middle MREE. In the primitive  
328 mantle-normalized multi-element diagram (Fig. 7b), patterns of the mafic lavas are bell  
329 shaped, as expected for OIB, and show strong negative anomalies in Rb, K and Pb, and, to a  
330 lesser extent, in U and Ti. Olivine melilitites – especially FL 386 – display high values in U,  
331 Sr, P, Nd, Sm, Eu and Gd. Olivine-free nephelinites have, on average, higher REE contents  
332 than the mafic rocks (Fig. 7c). Phonolites have characteristic concave-up REE patterns, with  
333 low MREE values, and LREE and HREE compositions close to those of mafic and  
334 intermediate rocks. The pumices of Petite Terre, which have the highest REE contents  
335 amongst the phonolites, show a negative anomaly in Eu. Olivine-free nephelinites and all  
336 evolved rocks display negative anomalies in P and Ti (Fig. 7d). Moreover, phonolites (lavas  
337 and pumices) are depleted in Ba and phonolitic pumices also in Sr.

338

### 339 *6.3. Isotopes*

340

341 A selection of Sr and Nd isotopic ratios and all the Pb data are given in Table 3. In the  
342  $^{207}\text{Pb}/^{204}\text{Pb}$  vs.  $^{206}\text{Pb}/^{204}\text{Pb}$  diagram of Figure 8a, there are evident relationships between the  
343 isotopic compositions of the samples and their geographic location and age. In fact, most of  
344 the lavas from the south and northwest shield volcanoes exhibit the most radiogenic  
345  $^{207}\text{Pb}/^{204}\text{Pb}$  ( $> 15.64$ ) and  $^{206}\text{Pb}/^{204}\text{Pb}$  ( $> 19.87$ ), whereas the post-shield north central domain  
346 lavas display the lowest ratios ( $^{207}\text{Pb}/^{204}\text{Pb} < 15.6$  and  $^{206}\text{Pb}/^{204}\text{Pb} < 19.35$ ). The post-shield  
347 Combani lavas, northwest olivine melilitites, and Petite Terre samples (xenolith PN5b apart)

348 show isotope ratios between these two groups but closer to north central lavas. This isotopic  
349 distribution seems to roughly reflect the volcanological history of the island. In general, lavas  
350 showing the most radiogenic Pb ratios have been sampled in the oldest parts of the island (>  
351 3.0 Ma), whereas the other samples belong to formations having an age < ~2.5 Ma. The only  
352 exceptions are the HIMU-flavored M25 and DMM-like M137 lavas, samples respectively  
353 dated to 2.0 and 5.0 Ma but for which no plateau age could be calculated (Table 1). There is  
354 also an uncertainty about the olivine melilitites (M66 and FL386), the age of which ranges  
355 from 4.0 to < 1.0 Ma. Even if the variations in the  $^{143}\text{Nd}/^{144}\text{Nd}$  vs.  $^{206}\text{Pb}/^{204}\text{Pb}$  diagram are less  
356 contrasted, similar trends can be observed. The  $^{143}\text{Nd}/^{144}\text{Nd}$  ratios of the rocks from the shield  
357 volcanoes, highly radiogenic in Pb, are more scattered and in average lower than those of the  
358 other samples. The  $^{87}\text{Sr}/^{86}\text{Sr}$  ratio is less discriminative (Table 3).

359         When compared to other Comores Islands and mantle end-member (Depleted MORB-  
360 Mantle: DMM; high  $^{238}\text{U}/^{204}\text{Pb}$ : HIMU; Enriched Mantle: EM1 and 2, of Zindler and Hart,  
361 1986) isotope compositions, the most recent lavas from Mayotte tend towards the depleted  
362 mantle, such as all the lavas produced by the La Grille volcano in Grande Comore and two  
363 samples from Moheli. In contrast, samples collected in the south and northwest shield  
364 volcanoes have a clear HIMU affinity, such as one sample from Moheli and all the lavas from  
365 Anjouan that have been analyzed for Pb isotopes.

366         The south alkali basalt M41, that spatially belongs to south group but that shows less  
367 silica-undersaturated composition, displays a Sr-Nd composition close to that of the Karthala  
368 volcano in Grande Comore, which tends toward the EM end-members (Table 3): its  
369  $^{143}\text{Nd}/^{144}\text{Nd}$  ratio is low (0.51272) and its  $^{87}\text{Sr}/^{86}\text{Sr}$  ratio especially high (0.70383). M41 is  
370 relatively fresh (LOI=1.1) and it has low Rb/Sr ratio (0.5) suggesting that its high  $^{87}\text{Sr}/^{86}\text{Sr}$   
371 ratio is a pristine characteristic. M41 sample has not been analyzed for Pb isotopes. As EM-



372 like composition is restricted to this sample in Mayotte, sampling date and location have been  
373 thoroughly checked and confirm the expression of EM mantle component in Mayotte.

374

#### 375 *6.4. Spatial and temporal distribution of the geochemical characteristics*

376

377 The lavas from the main building phase of the shield volcanoes (south and northwest  
378 domains) have more radiogenic Pb compositions than the post-shield rocks (Combani massif,  
379 north central domains and Petite Terre).

#### 380 *Shield units*

381 The lavas from the south shield are among the highest silica-undersaturated of the  
382 island (Fig. 4) including olivine-bearing and olivine-free nephelinites, basanites and  
383 phonolites. They have the highest CaO contents together with the northwestern melilitites  
384 (Fig. 6a), and include most of the Nlarnite samples (Table 2). The south shield lavas have a  
385 HIMU affinity, with high Pb isotope ratios (Fig. 8).

386 Most of the analyzed samples from the northwest shield are moderately silica-  
387 undersaturated mafic lavas, mainly basanites, with characteristic low incompatible trace  
388 element contents. They show a HIMU affinity (Fig. 8). The basanitic xenolith PN5b from  
389 Petite Terre (Table 2) shares the trace and isotopic signature of the northwest shield lavas.  
390 These features suggest that this sample could correspond to a lava from the northwest shield  
391 substratum, extracted during an explosive event and incorporated within the pumices.

#### 392 *Post-shield units*

393 The only olivine melilitites of Mayotte are emplaced in the northwest domain during a  
394 post-shield extensional phase.

395 The post-shield lavas from the north central domain are moderately silica-  
396 undersaturated. They follow linear evolutionary trends in major and trace element diagrams

397 from basalts/basanites to phonolites through tephrite/tephriphonolites (Fig. 6). All the  
398 petrological types have a similar isotopic composition (e.g., Nd isotope ratios ranging from  
399 0.51288 to 0.51290, Fig. 8b). Such features suggest that chemical variations in north central  
400 lavas reflect differentiation processes from melts generated from a rather homogeneous  
401 mantle source, more depleted than for the other lavas.

402 The Combani evolved samples follow the highly silica-understaturated trend in the TAS  
403 diagram (Fig. 4). They have, however, lower CaO with respect to highly silica-undersaturated  
404 intermediate and felsic lavas of the south domain (Fig. 6a). Both groups have also similar  
405 behavior in HREE vs. Th diagrams (Fig. 6g and Table 2), reflecting probably comparable  
406 modalities of crystal fractionation. However, the Combani lavas are close to those of the north  
407 central domain in Hf vs. Th (Fig. 6f) and they have specific high Nb contents (Fig. 6e).  
408 Amongst the post-shield lavas, they have the most radiogenic  $^{206}\text{Pb}/^{204}\text{Pb}$  values (Fig. 8).

409 The pumices of Petite Terre are phonolitic in composition. They belong to the  
410 moderately silica-undersaturated trend in the TAS diagram (Fig. 4) and plot in a restricted  
411 area of the trace element diagrams (Fig. 6e-g), away from all the other Mayotte samples.

412

## 413 **7. Discussion**

414

### 415 *7.1. Olivine melilitite genesis*

416

417 The olivine melilitites are ultracalcic mafic lavas, characterized by high contents in  
418 CaO and MgO; high silica-undersaturation, with SiO<sub>2</sub> contents < 40 wt.% (Wilson et al.,  
419 1995); low values in Al<sub>2</sub>O<sub>3</sub>, and, to a lesser extent, alkalis; and straight slopes in chondrite-  
420 normalized REE diagrams (Brey, 1978; Rogers et al., 1992; Wilson et al., 1995). Based on  
421 such chemical features, Brey (1978) and Rogers et al. (1992) have proposed that melilititic

422 primary magmas are generated by very low degree of partial melting of a garnet- (and  
423 phlogopite-?) bearing CO<sub>2</sub>-rich mantle source. Such low partial melting models for melilititic  
424 melts are consistent with the experimental works of Gudfinnsson and Presnall (2005). Wilson  
425 et al. (1995) and Melluso et al. (2011) have suggested that carbonates (probably dolomite)  
426 were involved in the melting process. From data of experimental petrology, Gudfinnsson and  
427 Presnall (2005) have positioned the field of the mantle at the origin of melilititic primary  
428 melts in the domain of garnet stability, in presence of CO<sub>2</sub>, at pressures ranging from 3 and 4  
429 GPa. Partial melting experiments of carbonated peridotite at 3 GPa generate melt  
430 compositions close to melilititic lavas (Hirose, 1997; Dasgupta et al., 2007), except for TiO<sub>2</sub>  
431 and FeO<sup>T</sup>, lower in these experimental melts than in natural olivine melilitites. To account for  
432 their geochemistry, Dasgupta et al. (2006, 2007) propose as melting source a carbonated  
433 peridotite metasomatized by pyroxenitic melts.

434 Besides the wide range of geochemical features listed above, the olivine melilitites of  
435 Mayotte present specific characteristics, namely high P<sub>2</sub>O<sub>5</sub> and Sr contents (Figs. 6d and 7b,  
436 and Table 2), and relative enrichments in MREE with respect to the other mafic rocks (Fig.  
437 7a). The sole other mention of P-rich melilitites has been made by Bailey et al. (2005) for  
438 Ugandan rocks. In the figure 6d diagram, it is shown that all the Nlarnite samples are enriched  
439 in P<sub>2</sub>O<sub>5</sub>. Consequently, to explore the melilititic character of the P-rich Nlarnite lavas, we have  
440 reported them in the P<sub>2</sub>O<sub>5</sub> vs. CaO/(SiO<sub>2</sub>+Al<sub>2</sub>O<sub>3</sub>) diagram of figure 9: the higher this ratio is,  
441 the more silica-undersaturated, CaO-rich and Al<sub>2</sub>O<sub>3</sub>-poor the rock is. The positive correlation  
442 demonstrates that a high P<sub>2</sub>O<sub>5</sub> content is also a melilititic feature in Mayotte. The P<sub>2</sub>O<sub>5</sub>  
443 enrichment of the Nlarnite lavas (Figs. 6d and 9), together with the relatively high Sr and  
444 MREE contents of both olivine melilitites (Table 2 and Fig. 7), is consistent with the  
445 hypothesis of an apatite contribution in the genesis of these lavas. Apatite can be involved  
446 through two mechanisms: (1) melting at very low degree of apatite-bearing pyroxenite veins

447 in lithospheric metasomatized mantle (Foley, 1992); (2) assimilation of apatite-bearing veins  
448 during the ascent of primary melts formed at a greater depth (Bailey et al., 2005). Scenario  
449 (1), implying small melting degrees, is consistent with the high silica-undersaturation of the  
450 N-larnite lavas, especially olivine melilitites. Both models imply a metasomatism episode, in  
451 which CO<sub>2</sub>-rich fluids or carbonatitic melts are probably involved (Hirschmann et al., 2003).  
452 This is consistent with the classic models of melilitite genesis (see references above) and with  
453 the occurrence in Grande Comore lavas of mantle xenoliths metasomatized by alkali-  
454 carbonatitic melt (Coltorti et al., 1999).

455

## 456 7.2. HIMU-flavored lavas

457

458 In order to minimize the effects of melt differentiation (crystallization, contamination)  
459 and to discuss the contribution of the mantle sources, this section focuses on relatively mafic  
460 lavas (MgO > 5 wt.%). As evidenced in Figure 8, the isotopic composition of Mayotte lavas is  
461 consistent with mixing between depleted mantle and HIMU components.

462 The HIMU-flavored mafic lavas, characterized by high Pb isotopic ratios, are reputed  
463 to be enriched in Nb and Ta and depleted in alkali/earth-alkali elements relative to the other  
464 incompatible trace elements (Dupuy et al., 1989; Willbold and Stracke, 2006). These features  
465 are noticeable in the HIMU-like olivine nephelinites collected in the south shield of Mayotte  
466 (Table 2 and Fig. 7b). Nevertheless, rocks from the northwest shield, which also have a clear  
467 HIMU isotopic signature, do not show these trace element features.

468 The HIMU mantle end-member is generally considered as the signature of a long-lived  
469 mantle reservoir (> 1 Ga). It has been ascribed to (1) a metasomatized mantle that has  
470 undergone a removal of Rb and Pb (Zindler and Hart, 1986) and/or an U enrichment through  
471 CO<sub>2</sub>-rich fluids (Nakamura and Tatsumoto, 1988); (2) an ancient subduction-modified

472 oceanic lithosphere, depleted in LILE as the result of dehydration (White and Hofmann, 1982;  
473 Dupuy et al., 1989); or (3) combination of both models, i.e. a peridotite metasomatized with  
474 carbonated silicate melts, carbonatites derived from a recycled oceanic crust (Jackson and  
475 Dasgupta, 2008) or carbonated eclogites (Dasgupta et al., 2010). The fact that the lavas from  
476 the northwest shield are not enriched in Ta and Nb (Table 2) is not really consistent with the  
477 model (2).

478 In Mayotte, only the oldest rocks show a HIMU signature. Contrary to some  
479 Marquesas examples as Ua Pou (Duncan et al., 1986; Legendre et al., 2005) and Eiao (Caroff  
480 et al., 1995), where the HIMU-like lavas have distinct petrographic and geochemical features  
481 compared to the other rocks, here, the isotopic composition is disconnected from the silica-  
482 undersaturation and elemental (major and trace elements) composition of the lavas, which  
483 precludes any connection between source composition and partial melting modalities.

484 The isotopic composition of Mayotte lavas is consistent with a mixing between DMM  
485 and HIMU end-members (Fig. 8). This feature has already been stated for the Canary  
486 Archipelago by Gurenko et al. (2009) and Aulinas et al. (2010). However, the HIMU-like  
487 lavas in Gran Canaria correspond to a post-shield phase (Aulinas et al., 2010), unlike  
488 Mayotte. Isotopic data for Canaries and Mayotte are both consistent with the assumption of  
489 small-scale HIMU heterogeneities in a depleted mantle (see section 7.3).

490 We compare the Nd/Yb vs. SiO<sub>2</sub> and Nd/Yb vs. Nb/Zr diagrams (Fig. 10) and the  
491 isotopic ratios (Fig. 8) in order to discriminate source composition, apatite contribution and  
492 melting degree. Apatite contribution during a deep metasomatism episode increases Nb/Yb  
493 ratio at constant Nb/Zr ratio and SiO<sub>2</sub> content. Decrease of melting degree induces a decrease  
494 of SiO<sub>2</sub> content and an increase of Nd/Yb and Nb/Zr ratios. From the data distribution in  
495 Figure 10, <sup>N</sup>larnite-bearing lavas would result from low partial melting degree of a  
496 metasomatized apatite-bearing mantle source, with (<sup>N</sup>larnite-bearing nephelinites) or without

497 (olivine melilitites) HIMU affinity (Fig. 8). South and northwest shield lavas would derive  
498 from a similar HIMU-like mantle source (Fig. 8) and their elemental distinction results from  
499 increase of the partial melting degree from south to northwest lavas. North central post-shield  
500 lavas derive from a more depleted mantle (Fig. 8), through higher melting degrees than lavas  
501 of the main building stage (Fig. 10).

502

### 503 *7.3. Genesis of Comores lavas*

504

505 Two groups of mantle source models below Comores are proposed, which imply  
506 interactions between melt issued (1) from an EM1-HIMU heterogeneous plume and a DMM  
507 metasomatized lithosphere (Deniel, 1998); and (2) from a homogeneous plume with a  
508 dominant EM1 signature and a DMM-HIMU metasomatized lithosphere (Class and  
509 Goldstein, 1994, 1997; Späth et al., 1996; Class et al., 1998). In the latter models, the HIMU  
510 component would be introduced in the Comorian mantle reservoir through delamination or  
511 thermal erosion of a continental lithosphere during the Gondwana break-up. This group of  
512 models is consistent with the geographic position of the Comores Archipelago between two  
513 HIMU-bearing continental blocks: Africa and Madagascar (Bell and Tilton, 2001; Melluso et  
514 al., 2011).

515 Our data are rather consistent with the second type of models for the mantle source  
516 below Mayotte (Fig. 11): clear DMM-HIMU mixing and quasi absence of EM1 compositions  
517 (except M41, Table 3). During the main building stage, partial melting of a DMM-HIMU  
518 CO<sub>2</sub>-metasomatized lithosphere produced the south and northwest shield melts, with lower  
519 partial melting degrees for the south lavas (Fig. 10). The melting processes occurred in the  
520 garnet stability field, as suggested by the presence of  $\text{N}^{\text{I}}$ larnite-bearing ultracalcic melts (Brey  
521 and Green, 1977). During the post-shield phase, the more isotopically depleted homogeneous

522 north central melts were formed through higher melting degrees. The other post-shield rocks  
523 have Nd and Pb isotopic features intermediate between this north central group and the lavas  
524 of the main building phase (Fig. 8). The progressive increase of the depleted component  
525 influence through time (Fig. 8), especially for the north central rocks (Fig. 10), can be related  
526 to a lower proportion of HIMU component in the mantle source or to a progressive dilution of  
527 the melts issued from fusible and small-sized HIMU heterogeneities when melt productivity  
528 increases. However, HIMU-flavored northwest lavas are produced by similar melting degrees  
529 as the depleted north central lavas. We thus propose that the isotopic signature of the post-  
530 shield north central lavas is related to a high partial melting of a source where the HIMU  
531 component would have been partially consumed during the main building stage. The olivine  
532 melilitites would be generated from a source isotopically equivalent, but enriched in CO<sub>2</sub> and  
533 P<sub>2</sub>O<sub>5</sub> (probably with modal dolomite ± apatite) and with a low degree of partial melting. The  
534 most plausible lithologies for generating the silica-undersaturated primary melts of Mayotte  
535 lavas are carbonated garnet peridotite (Hirose, 1997; Dasgupta et al., 2007) and/or silica-  
536 deficient garnet pyroxenite/eclogite (Hirschmann et al., 2003, Dasgupta et al., 2010; Le Roux  
537 et al., 2011). Considering that the HIMU signature of the rocks is disconnected from partial  
538 melting modalities and that the Mayotte lavas, more or less fractionated, are not primary  
539 magmas, it would be difficult to go further in characterization of the source lithology.

540         The model of a depleted lithospheric mantle with HIMU small-scale heterogeneities  
541 can be extended to the other islands of the Comores archipelago. Indeed, the mixing trend  
542 DMM-HIMU is clear for Moheli, Anjouan and “La Grille”-type lavas from Grande Comore  
543 (Fig. 8). Nevertheless, the “Karthala”-type recent lavas from Grande Comore show a specific  
544 EM1 signature ( $^{87}\text{Sr}/^{86}\text{Sr} > 0.70350$  and  $^{143}\text{Nd}/^{144}\text{Nd} < 0.51275$ ). Class et al (1998) argued that  
545 the “Karthala”-type lavas result from mixtures between plume and lithosphere melts. Thus,  
546 we propose that Comores lavas are mainly generated by partial melting of a DMM-HIMU

547 CO<sub>2</sub>-metasomatized lithospheric mantle. The EM1 Comorian mantle plume would just have a  
548 thermal effect, except for the “Karthala”-type lavas – and for the Mayotte basalt M41,  
549 exhibiting an equivalent Sr-Nd isotopic composition – which probably resulted from  
550 plume/lithosphere interactions (Fig. 11).

551

## 552 **8. Concluding remarks**

553

554 The new set of geochronological and geochemical data presented in this study is used  
555 to discuss the chemistry and the mineralogy of the mantle source below Mayotte. The two  
556 main results are: (1) the characterization for the first time in the Comores of melilite-bearing  
557 lavas, including two olivine melilitites; and (2) the clear evidence of a HIMU signature in the  
558 shield lavas. Both features may or may not concern same samples.

559 Without doubt, the melting mantle source involved in the genesis of the Mayotte lavas  
560 is chemically and mineralogically heterogeneous at small scale. The HIMU affinity could find  
561 its origin in lithospheric components metasomatized by CO<sub>2</sub>-rich fluids, whereas melilite-  
562 bearing lavas would derive from partial melting at very low degree of a mantle source,  
563 isotopically similar or not, bearing modal carbonate and apatite. Time-increasing partial  
564 melting during the main building phase of the shield volcanoes would favor the expression in  
565 the post-shield lavas of a more depleted mantle signature, as the consequence of the dilution  
566 of the HIMU heterogeneities in the mantle, maybe coupled with their partial consumption  
567 during the shield phase.

568 Petrological and geochemical data can thus be used to draw a composite picture of the  
569 mantle below Mayotte, which probably changes with time. Regardless of what lavas are  
570 concerned, the melting lithosphere below Mayotte presents a general characteristic feature,  
571 which reconciles both isotopic and mineralogical data: it has undergone CO<sub>2</sub>-metasomatism.



572

573 **Acknowledgements**

574 Field studies were conducted in 2001 with the financial support of the Conseil  
575 Régional de La Réunion and the Laboratoire GéoSciences Réunion, and in 2010 and 2011  
576 with the financial and logistic support of the BRGM (Bureau de Recherches Géologiques et  
577 Minières) and with the participation of F. Lacquement and J. Bernard. ISTERRE is part of Labex  
578 OSUG@2020 (ANR10 LABX56). The authors are grateful to J. Langlade and V. Batanova  
579 (microprobe analyses), C. Bollinger (ICP-MS Brest), Ph. Nonnotte (TI-MS), C. Liorzou (ICP-  
580 AES), Y. Germain (MC-ICP-MS Ifremer), and P. Tiffenbach (thin sections). Detailed and  
581 constructive remarks by Drs Meritxell Aulinas and Hannes B. Mattsson helped us a lot to  
582 improve the manuscript. We also thank Dr Nelson Eby for his editorial assistance.

583

584 **Appendix. Supplementary Table S1.**

585 Supplementary data to this article can be found online at doi:  
586

587 **References**

588

- 589 Arnaud, N., Tapponnier, P., Roger, F., Brunel, M., Scharer, U., Wen, C. and Zhiqin, X., 2003.  
590 Evidence for Mesozoic shear along the western Kunlun and Altyn-Tagh fault, northern  
591 Tibet (China). *Journal of Geophysical Research*, 108(B1), 2053,  
592 doi:10.1029/2001JB000904.
- 593 Audru, J.C., Guennoc, P., Thinon, I., Abellard, O., 2006. Bathymay: la structure sous-marine  
594 de Mayotte révélée par l'imagerie multifaisceaux. *Compte Rendus Geoscience* 338,  
595 1240-1249.

- 596 Aulinas, M., Gimeno, D., Fernandez-Turiel, J.L., Font, L., Perez-Torrado, F.J., Rodriguez-  
597 Gonzalez, A., Nowell, G.M., 2010. Small-scale mantle heterogeneity on the source of  
598 the Gran Canaria (Canary Islands) Pliocene-Quaternary magmas. *Lithos* 119, 377-392.
- 599 Barrat, J.-A., Keller, F., Amossé, J., Taylor, R.N., Nesbitt, R.W., Hirata, T., 1996.  
600 Determination of rare earth elements in sixteen silicate reference samples by ICP-MS  
601 after Tm addition and ion exchange separation. *Geostandards Newsletters* 20, 133-139.
- 602 Barrat, J.-A., Zanda, B., Moynier, F., Bollinger, C., Liorzou, C., Bayon, G., 2012.  
603 Geochemistry of CI chondrites: Major and trace elements, and Cu and Zn isotopes.  
604 *Geochimica et Cosmochimica Acta* 83, 79-92.
- 605 Bailey, K., Lloyd, F., Kearns, S., Stoppa, F., Eby, N., Woolley, A., 2005. Melilitite at Fort  
606 Portal, Uganda. Another dimension of the carbonate volcanism. *Lithos* 85, 15-25.
- 607 Bell, K., Tilton, G.R., 2001. Nd, Pb and Sr isotopic compositions of East African  
608 carbonatites: evidence for mantle mixing and plume inhomogeneity. *Journal of*  
609 *Petrology* 42, 1927-1945.
- 610 Bertil, D., Regnault, J.M., 1998. Seismotectonic of Madagascar. *Tectonophysics* 294, 57-74.
- 611 Brey, G., 1978. Origin of olivine melilitites – chemical and experimental constraints. *Journal*  
612 *of Volcanology and Geothermal Research* 3, 61-88.
- 613 Brey, G., Green, D.H., 1977. Systematic study of liquidus phase relations in olivine melilitite  
614 + H<sub>2</sub>O + CO<sub>2</sub> at high pressures and petrogenesis of an olivine melilitite magma.  
615 *Contributions to Mineralogy and Petrology* 61, 141-162.
- 616 Camoin, G.F., Montaggioni, L.F., Braithwaite, C.J.R., 2004. Late glacial to post glacial sea  
617 levels in the Western Ocean. *Marine Geology* 206, 119–146.
- 618 Caroff, M., Maury, R.C., Vidal, Ph., Guille, G., Dupuy, C., Cotten, J., Guillou, H., Gillot, P.-  
619 Y., 1995. Rapid temporal changes in Ocean Island Basalt composition: evidence from a  
620 800 m-deep drill hole in Eiao shield (Marquesas). *Journal of Petrology* 36, 1333-1365.

- 621 Chauvel, C., Bureau, S., Poogi, C., 2011. Comprehensive chemical and isotopic analyses of  
622 basalt and sediment reference materials. *Geostandards and Geoanalytical Research*. 35,  
623 125-143.
- 624 Class, C., Goldstein, S.L., 1994. Ocean island basalts and lithospheric melting: constraints  
625 from the source mineralogy. V.M. Goldschmidt Conference, Edimburgh, Abstr. Vol., p.  
626 175.
- 627 Class, C., Goldstein, S.L., 1997. Plume-lithosphere interactions in the ocean basins:  
628 constraints from the source mineralogy. *Earth Planet. Sci. Lett.* 150, 245-260.
- 629 Class, C., Goldstein, S.L., Altherr, R., Bachelery, P., 1998. The process of Plume -  
630 Lithosphere interactions in the Ocean Basins - The case of Grande Comore. *Journal of*  
631 *Petrology* 39, 881-903.
- 632 Class, C., Goldstein, S.L., Shirey, S.B., 2009. Osmium isotopes in Grande Comore lavas: a  
633 new extreme among a spectrum of EM-type mantle endmembers. *Earth and Planetary*  
634 *Science Letters* 284, 219-227.
- 635 Class, C., Goldstein, S.L., Stute, M., Kurz, M., Schlosser, P., 2005. Grande Comore island: a  
636 well-constrained low  $3\text{He}/4\text{He}$  mantle plume. *Earth and Planetary Science Letters* 233,  
637 391-409.
- 638 Coltorti, M., Bonadiman, C., Hinton, R.W., Siena, F., Upton, B.G.J., 1999. Carbonatite  
639 metasomatism of the oceanic upper mantle: evidence from clinopyroxenes and glasses  
640 in ultramafic xenoliths of Grande Comore, Indian Ocean. *Journal of Petrology* 40, 133-  
641 165.
- 642 Cotten, J., Le Dez, A., Bau, M., Caroff, M., Maury, R.C., Dulski, P., Fourcade, S., Bohn, M.,  
643 Brousse, R., 1995. Origin of anomalous rare-earth elements and yttrium enrichments in  
644 sub-aerially exposed basalts: evidence from French Polynesia. *Chemical Geology* 119,  
645 115-138.

- 646 Dasgupta, R., Hirschmann, M.M., Smith, N.D., 2007. Partial melting experiments of  
647 peridotite + CO<sub>2</sub> at 3 GPa and genesis of alkali ocean island basalts. *Journal of*  
648 *Petrology* 48, 2093-2124.
- 649 Dasgupta, R., Jackson, M.G., Lee, C.-T.A., 2010. Major element chemistry of ocean island  
650 basalts – Conditions of mantle melting and heterogeneity of mantle source. *Earth and*  
651 *Planetary Science Letters* 289, 377-392.
- 652 Dasgupta, R., Hirschmann, M.M., Stalker, K., 2006. Immiscible transition from carbonate-  
653 rich to silicate-rich melts in the 3 GPa melting interval of eclogite + CO<sub>2</sub> and genesis of  
654 silica-undersaturated ocean island lavas. *Journal of Petrology* 47, 647-671.
- 655 Dautria, J.M., Dupuy, C., Takherist, D., Dostal, J., 1992. Carbonate metasomatism in the  
656 lithospheric mantle: peridotitic xenoliths from a melilititic district of the Sahara basin.  
657 *Contributions to Mineralogy and Petrology* 111, 37-52.
- 658 Dawson, J.B., 2012. Nephelinite-melilitite-carbonatite relationships: Evidence from  
659 Pleistocene-recent volcanism in northern Tanzania. *Lithos* 152, 3-10.
- 660 Debeuf, D., 2004. Etude de l'évolution volcano-structurale et magmatique de Mayotte  
661 (Archipel des Comores, Océan Indien). Thesis, University of La Réunion, 277 pp.
- 662 Deniel, 1998. Geochemical and isotopic (Sr, Nd, Pb) evidence for the plume-lithosphere  
663 interactions in the genesis of Grande Comore magmas (Indian Ocean). *Chemical*  
664 *Geology* 144, 281-303.
- 665 Duncan, R. A., McCulloch, M. T., Barszczus, H. G., Nelson, D. R., 1986. Plume vs  
666 lithospheric melts at Ua Pou, Marquesas Islands. *Nature* 322, 534-538.
- 667 Dupré, B., Allègre, C.-J., 1983. Pb-Sr isotope variation in Indian Ocean basalts and mixing  
668 phenomena. *Nature* 303, 142-146.

- 669 Dupuy, C., Barszczus, H.G., Dostal, J., Vidal, P., Liotard, J.M., 1989. Subducted and recycled  
670 lithosphere as the mantle source of ocean island basalts from southern Polynesia, central  
671 Pacific. *Chemical Geology* 77, 1-18.
- 672 Emerick, C.M., Duncan, R.A., 1982. Age progressive volcanism in the Comores Archipelago,  
673 western Indian Ocean and implications for Somali plate tectonics. *Earth and Planetary  
674 Science Letters* 60, 415-428.
- 675 Fleck, F.J., Sutter, J.F., Elliot, D.H., 1977. Interpretation of discordant  $^{40}\text{Ar}/^{39}\text{Ar}$  age spectra  
676 of Mesozoic tholeiites from Antarctica. *Geochimica et Cosmochimica Acta*, 41, 15-32.
- 677 Foley, S., 1992. Vein-plus-wall-rock melting mechanisms in the lithosphere and the origin of  
678 potassic alkaline magmas. *Lithos* 28, 435-453.
- 679 Garcia, S., Arnaud, N.O., Angelier, J., Françoise, B., Homberg, C., 2003. Rift jump process in  
680 northern Iceland since 10 Ma from  $^{40}\text{Ar}/^{39}\text{Ar}$  geochronology. *Earth and Planetary  
681 Science Letters* 214, 529–544.
- 682 Gudfinnsson, G.H., Presnall, D.C., 2005. Continuous gradations among primary carbonatitic,  
683 kimberlitic, melilititic, basaltic, picritic and komatiitic melts in equilibrium with garnet  
684 lherzolite at 3-8 GPa. *Journal of Petrology* 46, 1645-1659.
- 685 Gurenko, A.A., Sobolev, A.V., Hoernle, K.A., Hauff, F., Schmincke, H.-U., 2009. Enriched,  
686 HIMU-type peridotite and depleted recycled pyroxenite in the Canary plume: A mixed-  
687 up mantle. *Earth and Planetary Science Letters* 277, 514-524.
- 688 Hajash, A., Armstrong, R.L., 1972. Paleomagnetic and radiometric evidence for the age of the  
689 Comores Islands, West Central Indian Ocean. *Earth and Planetary Science Letters* 16,  
690 231-236.
- 691 Hirschmann, M.M., Kogiso, T., Baker, M.B., Stolper, E.M., 2003. Alkalic magmas generated  
692 by partial melting of garnet pyroxenite. *Geology* 31, 481-484.

- 693 Hirose, K., 1997. Partial melt compositions of carbonated peridotite at 3 GPa and role of CO<sub>2</sub>  
694 in alkali-basalt magma generation. *Geophysical Research Letters* 24 (22), 2837-2840.
- 695 Hoernle, K., Schmincke, H.-U., 1993. The petrology of the tholeiites through the melilite  
696 nephelinites on Gran Canaria, Canary Islands: crystal fractionation, accumulation and  
697 depths of melting. *Journal of Petrology* 34, 573-597.
- 698 Janney, P.E., Le Roex, A.P., Carlson, R.W., Viljoen, K.S., 2002. A chemical and multi-  
699 isotope study of the Western Cape olivine melilitite province, South Africa: implications  
700 for the sources of kimberlites and the origine of the HIMU signature in Africa. *Journal*  
701 *of Petrology* 43, 2339-2370.
- 702 Jackson, M.G., Dasgupta, R., 2008. Compositions of HIMU, EM1 and EM2 from global  
703 trends between radiogenic isotopes and major elements in ocean island basalts. *Earth*  
704 *and Planetary Science Letters* 276, 175-186.
- 705 Le Bas, M.J., 1989. Nephelinitic and basanitic rocks. *J. Petrol.* 30, 1299-1313.
- 706 Le Bas, M.J., Le Maitre, R.W., Streckeisen, A., Zanettin, B., 1986. A chemical classification  
707 of volcanic rocks based on the total alkali-silica diagram. *Journal of Petrology* 27, 745-  
708 750.
- 709 Leclaire, L., Bassias, Y., Clocchiatti, M., Ségoufin, J., 1989. La ride de Davie dans le canal de  
710 Mozambique : approche stratigraphique et géodynamique. *Comptes Rendus de*  
711 *l'Académie des Sciences, Paris* 308, 1077-1089.
- 712 Legendre, C., Maury, R.C., Caroff, M., Guillou, H., Cotten, J., Chauvel, C., Bollinger, C.,  
713 Hémond, C., Guille, G., Blais, S., Rossi, P., Savanier, D., 2005. Origin of exceptionally  
714 abundant phonolites on Ua Pou Island (Marquesas, French Polynesia): Partial melting of  
715 basanites followed by crustal contamination. *Journal of Petrology* 46, 1925-1962.

- 716 Le Roux, V., Dasgupta, R., Lee, C.-T.A., 2011. Mineralogical heterogeneities in the Earth's  
717 mantle: Constraints from Mn, Co, Ni and Zn partitioning during partial melting. *Earth  
718 and Planetary Science Letters* 307, 395-408.
- 719 Maaløe, S., James, D., Smedley, P., Petersen, S., Gramann, L.B., 1992. The Koloa volcanic  
720 suite of Kauai, Hawaii. *Journal of Petrology* 33, 761-784.
- 721 Malod, J.A., Mougnot, D., Raillard, S., Maillard, A., 1991. Nouvelles contraintes sur la  
722 cinématique de Madagascar : les structures de la chaîne de Davie. *Comptes Rendus de  
723 l'Académie des Sciences, Paris* 312, 211-214.
- 724 Mattsson, H.B., Nandedkar, R.H., Ulmer, P., 2013. Petrogenesis of the melititic and  
725 nephelinitic rock suites in the Lake Natron – Engaruka monogenetic volcanic field,  
726 northern Tanzania. *Lithos* 179, 175-192.
- 727 McDonough, W.F., Sun, S.-S., 1995. The composition of the Earth. *Chemical Geology* 120,  
728 223-253.
- 729 Médard, E., Schmidt, M.W., Schiano, P., 2004. Liquidus surfaces of ultracalcic primitive  
730 melts: formation conditions and sources. *Contributions to Mineralogy and Petrology*  
731 148, 201-215.
- 732 Melluso, L., Le Roex, A.P., Morra, V., 2011. Petrogenesis and Nd-, Pb-, Sr-isotope  
733 geochemistry of the Cenozoic olivine melilitites and olivine nephelinites (“ankaratrites”)  
734 in Madagascar. *Lithos* 127, 505-521.
- 735 Nakamura, Y., Tatsumoto, M., 1988. Pb, Nd and Sr isotopic evidence for a multi-component  
736 source for rocks of the Cook-Austral Islands and heterogeneities of mantle plumes.  
737 *Geochimica et Cosmochimica Acta* 52, 2909-2924.
- 738 Nehlig, P., Lacquement, F., Bernard, J., Caroff, M., Deparis, J., Jaouen, T., Pelleter, A.-A.,  
739 Perrin, J., Prognon, C., Vittecoq, B., 2013. Notice de la carte géologique de Mayotte à  
740 1/25 000, BRGM/RP-61803-FR. BRGM Éditions, Orléans.

- 741 Nougier, J., Cantagrel, J.-M., Karche, J.P., 1986. The Comores archipelago in the western  
742 Indian Ocean: volcanology, geochronology and geodynamic setting. *Journal of African*  
743 *Earth Sciences* 5, 135-145.
- 744 Piqué, A., 1999. L'évolution géologique de Madagascar et la dislocation du Gondwana : une  
745 introduction. *Journal of African Earth Sciences* 28 (4), 919-930.
- 746 Reisberg, L., Zindler, A., Marcantonio, F., White, W., Wyman, D., Weaver, B., 1993. Os  
747 isotope systematics in ocean island basalts. *Earth and Planetary Science Letters* 120,  
748 149-167.
- 749 Renne, .R., Swisher, C.C., Deino, A.L., Karner, D.b., Owens, T.I., DePaolo, D.J., 1998.  
750 Intercalibration of standards, absolute ages and uncertainties in  $Ar^{40}/Ar^{39}$  dating.  
751 *Chemical Geology* 145, 117-152.
- 752 Roddick, J.C., Cliff, R.A., Rex, D.C., 1980. The evolution of excess argon in alpine biotites—  
753 an  $^{40}Ar-^{39}Ar$  analysis. *Earth and Planetary Science Letters* 48, 185–208.
- 754 Rogers, N.W., Hawkesworth, C.J., Palacz, Z.A., 1992. Phlogopite in the generation of  
755 olivine-melilitites from Namaqualand, South Africa and implications for element  
756 fractionation processes in the upper mantle. *Lithos* 28, 347-365.
- 757 Salters, V.J.M., White, W.M., 1998. Isotope constraints on mantle evolution. *Chemical*  
758 *Geology* 145, 447-460.
- 759 Späth, A., Le Roex, A.P., Duncan, R.A., 1996. The geochemistry of lavas from the Comores  
760 Archipelago, western Indian Ocean: petrogenesis and mantle source region  
761 characteristics. *Journal of Petrology* 37 (4), 961-994.
- 762 Stieltjes, L., 1988. Notice explicative de la carte géologique de Mayotte à 1/50 000. BRGM  
763 Éditions, Orléans.



- 764 Suschevskaya, N.M., Kamenetsky, V.S., Belyatsky, B.V., Artamonov, A.V., 2013.  
765 Geochemical evolution of Indian Ocean basaltic magmatism. *Geochemistry*  
766 *International* 51 (8), 599-622.
- 767 Tindle, A.G., Webb, P.C., 1994. Probe-Amph-A spreadsheet program to classify microprobe  
768 derived amphibole analyses. *Computer & Geosciences* 20 (7/8), 1201-1228.
- 769 White, W.M., Hofmann, A.W., 1982. Sr and Nd isotope geochemistry of oceanic basalts and  
770 mantle evolution. *Nature* 296, 821-825.
- 771 Willbold, M., Stracke, A., 2006. Trace element composition of mantle end-members :  
772 Implications for recycling of oceanic and upper and lower continental crust.  
773 *Geochemistry Geophysics Geosystems* 7, Q04004, doi : 10.1029/2005GC001005.
- 774 Wilson, M. Rosembaum, J.M., Dunworth, E.A., 1995. Melilitites: partial melts of the thermal  
775 boundary layer? *Contributions to Mineralogy and Petrology* 119, 181-196.
- 776 Wooley, A.R. et al., 1996. Classification of lamprophyres, lamproites, kimberlites and th  
777 kalsitic, melilitic and leucitic rocks. *The Canadian Mineralogist* 34, 175-186.
- 778 York, D., 1969. Least square fitting on a straight line with correlated errors, *Earth and*  
779 *Planetary Science Letters* 5, 320-324.
- 780 Zindler, A., Hart, S., 1986. Chemical geodynamics. *Annual Review of Earth and Planetary*  
781 *Sciences* 14, 493-571.
- 782 Zinke, J., Reijmer, J.J.G., Thomassin, B.A., 2003. Systems tracts sedimentology in the lagoon  
783 of Mayotte associated with the Holocene transgression. *Sedimentary Geology* 160, 57-  
784 79.

785

786 **Figure captions**

787

788 Fig. 1. The Comores archipelago. K-Ar age ranges are indicated for each island: Grande  
 789 Comore (2 data by Hajash and Armstrong, 1972, and Emerick and Duncan, 1982); Moheli (12  
 790 data by Emerick and Duncan, 1982, and Nougier et al., 1986); Anjouan (8 data by Hajash and  
 791 Armstrong, 1972, Emerick and Duncan, 1982, and Nougier et al., 1986); Mayotte (34 data by  
 792 Hajash and Armstrong, 1972, Emerick and Duncan, 1982, and Nougier et al., 1986, and one  
 793 relative age determined by Zinke et al., 2003, for a pumice layer interbedded in the lagoon  
 794 stratigraphic succession). The value of 11.1 Ma of Anjouan corresponds to a remote value  
 795 measured on a syenitic xenolith. The Mayotte new age range of Table 1 is indicated in italic.  
 796 Inset: Mayotte in its geodynamical context.

797  
 798 Fig. 2. Geophysical and geological maps of Mayotte. (a) Bathymetry (from Audru et al.,  
 799 2006). (b) Digital terrain model (DTM) of Mayotte (Nehlig et al., 2013); mounts: 1. Mlima  
 800 Dziani Bolé (472 m); 2. Mlima Digo (255 m); 3. Mlima Mtsapéré (572 m); 4. Mlima  
 801 Combani (477 m); 5. Mlima Bénara (660 m); 6. Mlima Choungui (594 m). (c) Geological  
 802 sketch of Mayotte, based on Debeuf (2004) and Nehlig et al. (2013); the main four domains  
 803 (south, northwest, north central, Petite Terre), limited by bold dashed lines, have been defined  
 804 from topographic, geochronological, petrographic and geochemical criteria; M&I rocks: mafic  
 805 and intermediate rocks; samples listed in Tables 1 and 2 are positioned. (d) Volcanological  
 806 sketch of Petite Terre, showing tuff ring structures.

807  
 808 Fig. 3. Summary of petrographic data for Mayotte lavas: mineral occurrence and their  
 809 compositional range. NC: north central domain; Fo: forsterite; Wo: wollastonite; En: enstatite;  
 810 Ne: nepheline; An: anorthite; Or: orthoclase; Aegir.-augite: aegirine-augite; Fe-arfv.: ferro-  
 811 arfvedsonite; Fe-ecker.: ferro-eckermannite. Nomenclature of amphiboles based on Tindle  
 812 and Webb (1994).

813

814 Fig. 4. Total alkali-silica (TAS) discrimination diagram for lavas and pumices from Mayotte  
815 (weight percent). The fields are from Le Bas et al. (1986). For this diagram, major element  
816 values were recalculated to 100% in a free water basis. The Combani samples (south domain)  
817 are identified by a bold half circle.

818

819 Fig. 5. Nephelinite-melilitite-basanite classification diagram of Le Bas (1989) for mafic lavas  
820 ( $\text{MgO} > 5 \text{ wt.}\%$ ) from Mayotte (weight percent). Inset: olivine melilitite-nephelinite  
821 discrimination diagram of Wooley et al. (1996), same samples. Symbols as in figure 4.

822

823 Fig. 6. Variation of  $\text{CaO}$ ,  $\text{Al}_2\text{O}_3$ ,  $\text{K}_2\text{O}$  and  $\text{P}_2\text{O}_5$  vs.  $\text{MgO}$  (weight percent) and Nb, Hf, Yb and  
824 Nb/Zr vs. Th (ppm) for lavas and pumices from Mayotte. Symbols as in figure 4.

825

826 Fig. 7. Trace element patterns of representative Mayotte samples. (a) and (b): mafic lavas  
827 ( $\text{MgO} > 5 \text{ wt.}\%$ ); (c) and (d): intermediate nephelinites and phonolites. (a) and (c): chondrite-  
828 normalized REE patterns (normalization values: Barrat et al., 2012); (b) and (d): primitive  
829 mantle-normalized incompatible trace element patterns (normalization values: McDonough  
830 and Sun, 1995).

831

832 Fig. 8. (a)  $^{143}\text{Nd}/^{144}\text{Nd}$  vs.  $^{206}\text{Pb}/^{204}\text{Pb}$  and (b)  $^{207}\text{Pb}/^{204}\text{Pb}$  vs.  $^{206}\text{Pb}/^{204}\text{Pb}$  isotope diagrams  
833 showing Mayotte data compared with previously published data (Grande Comore: Dupré and  
834 Allègre, 1983; Reisberg et al., 1993; Späth et al., 1996; Class and Goldstein, 1997; Class et  
835 al., 1998; Deniel, 1998; Class et al., 2005; Class et al., 2009; Anjouan: Reisberg et al, 1993;  
836 Salters and White, 1998; Moheli: Reisberg et al., 1993; Späth et al., 1996). The position of the

837 DMM, EM I and II, and HIMU end-members are from Zindler and Hart (1986). Symbols as  
838 in figure 4.

839

840 Fig. 9.  $P_2O_5$  vs.  $CaO/SiO_2$  (wt. %) diagram for the N-larnite lavas. Symbols as in figure 4.

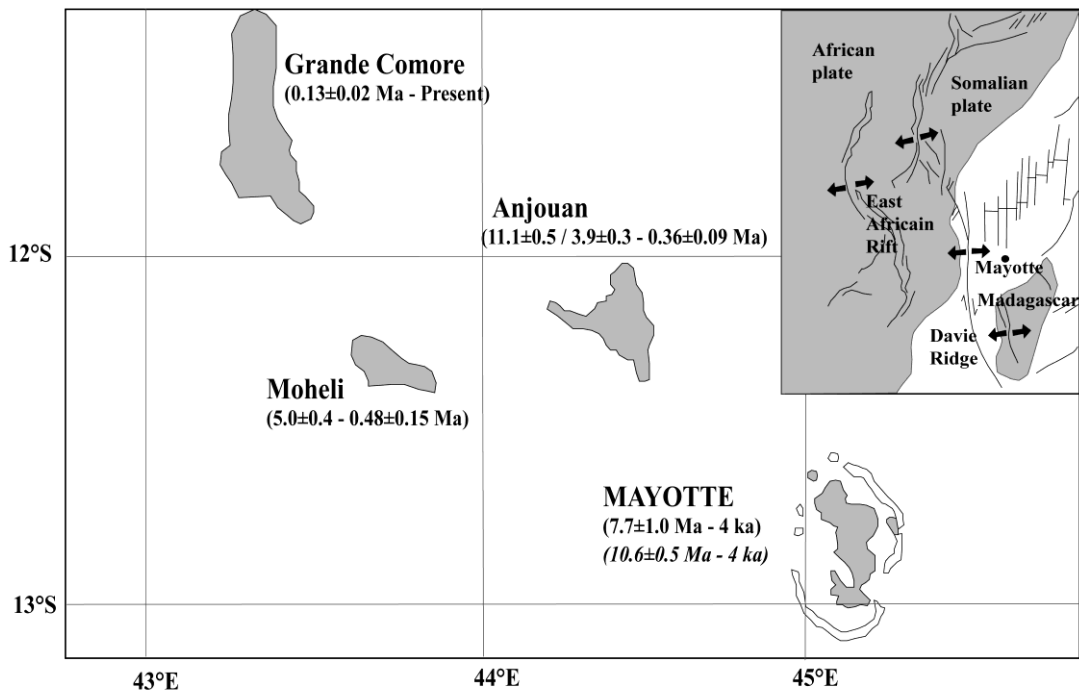
841

842 Fig. 10. (a) Nd/Yb (ppm) vs.  $SiO_2$  (wt. %) and (b) Nd/Yb vs. Nb/Zr (ppm) diagrams for the  
843 basic lavas from Mayotte. PM: partial melting. The grey areas correspond to HIMU-flavored  
844 lava samples ( $^{206}Pb/^{204}Pb > 19.87$ ).

845

846 Fig. 11. Schematic model showing the mantle structure below Mayotte during its main  
847 building phase. Partial melting of a DMM-HIMU  $CO_2$ -metasomatized lithosphere produced  
848 the south and northwest shield melts, with lower partial melting degrees for the south lavas.  
849 The melting processes occurred in the garnet stability field.

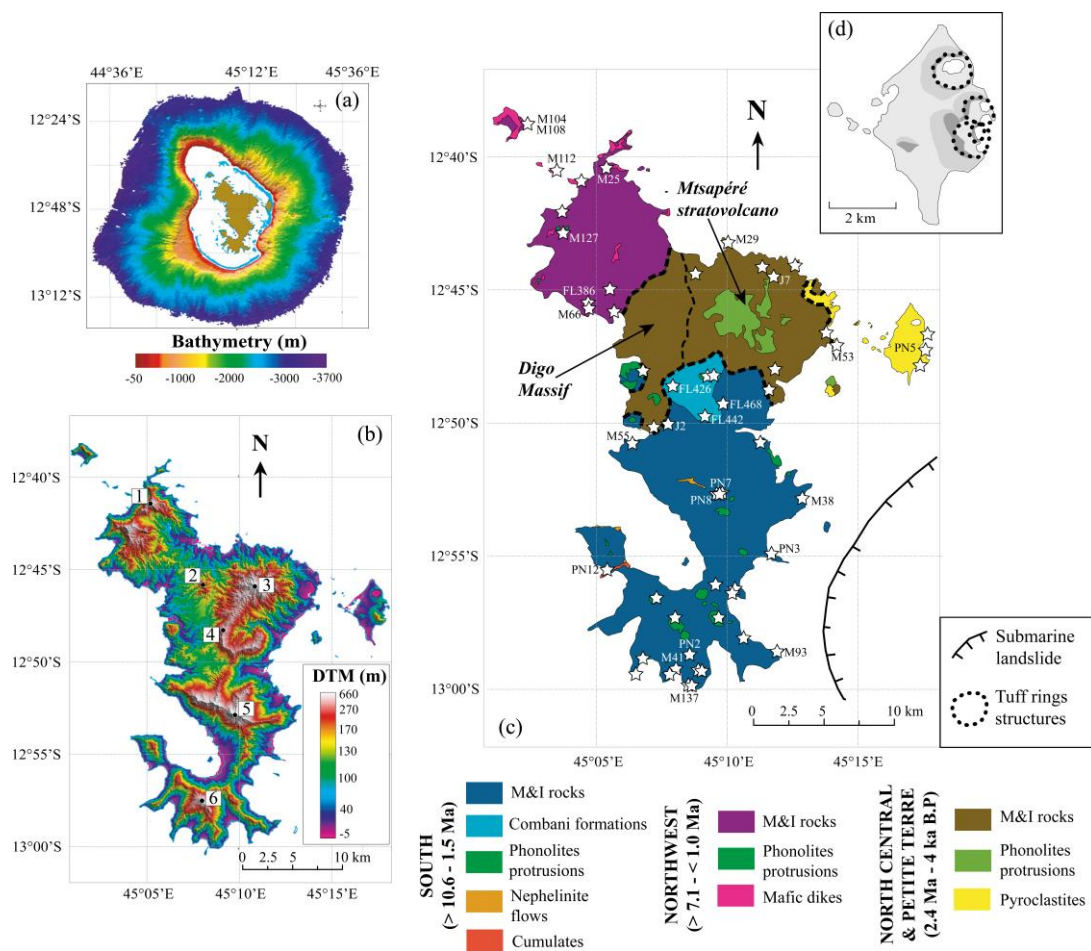
850



Pelleter et al. Fig. 1

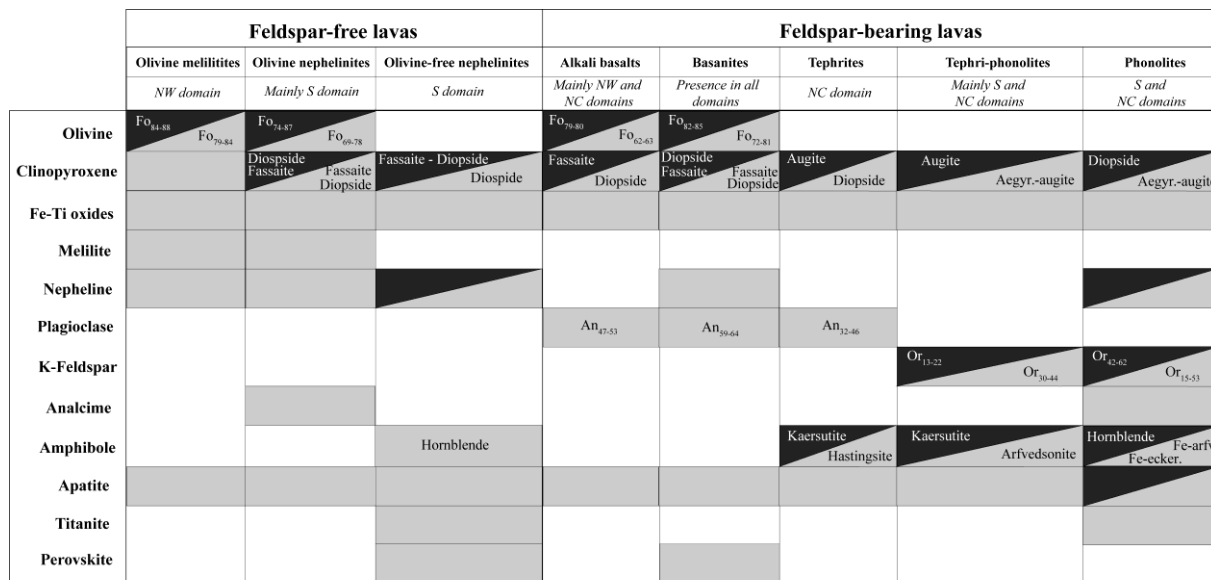
851

852



853

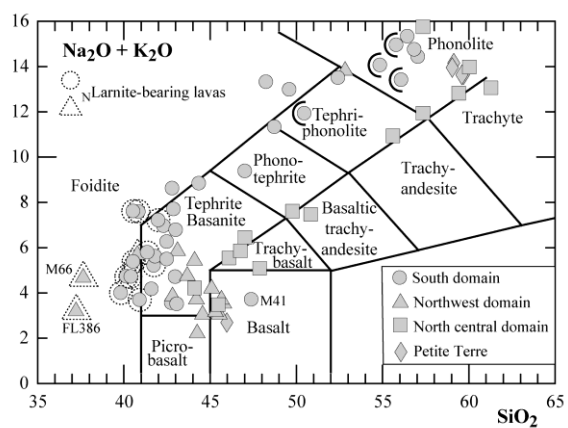
854 Fig. 2



855

■ Phenocrysts      ■ Groundmass

856 Fig. 3

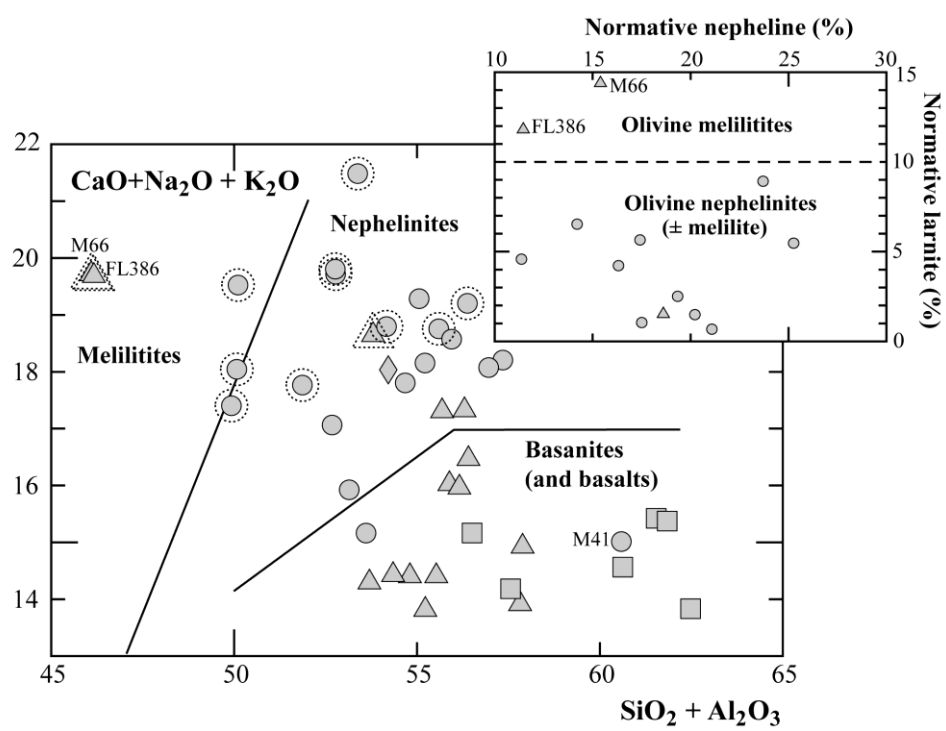


857

858

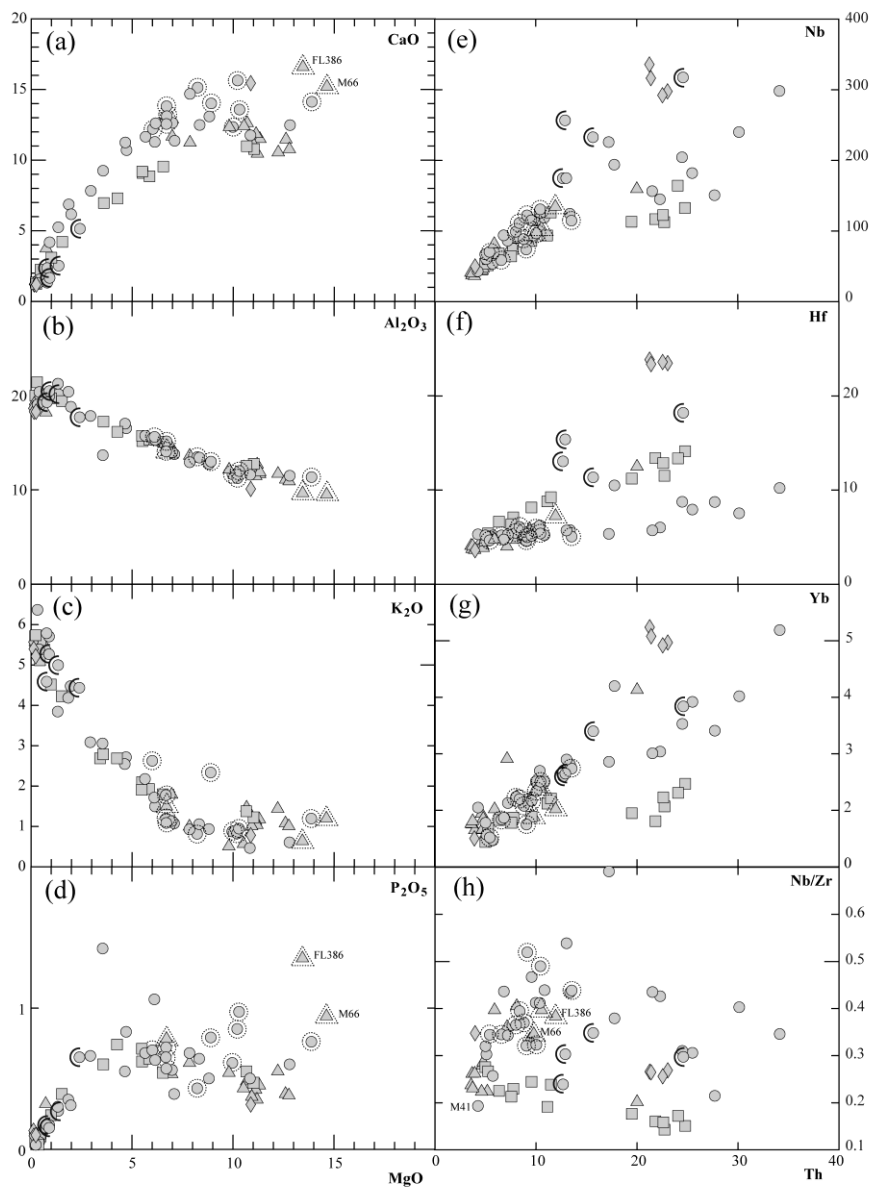
859 Fig. 4





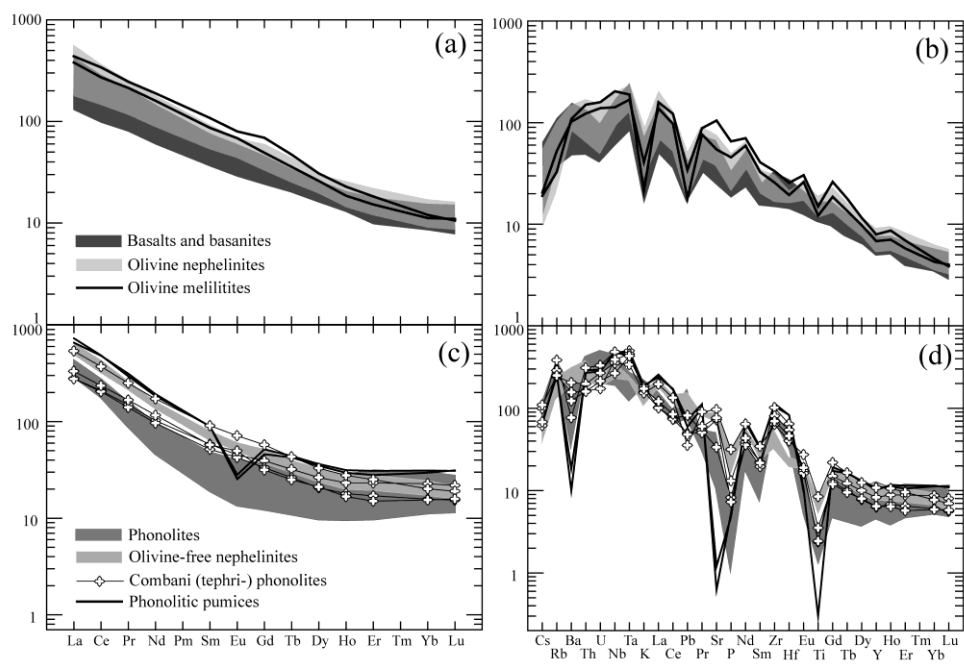
860

861 Fig. 5



862

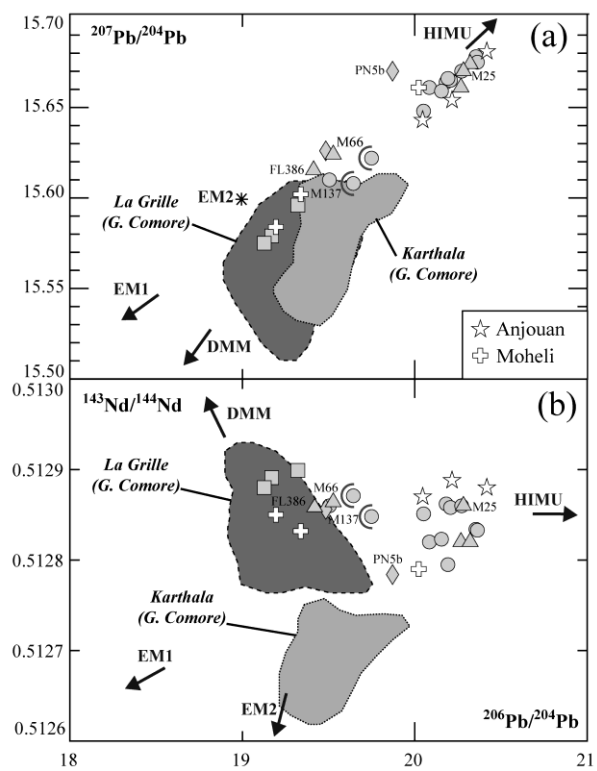
863 Fig. 6



864

865

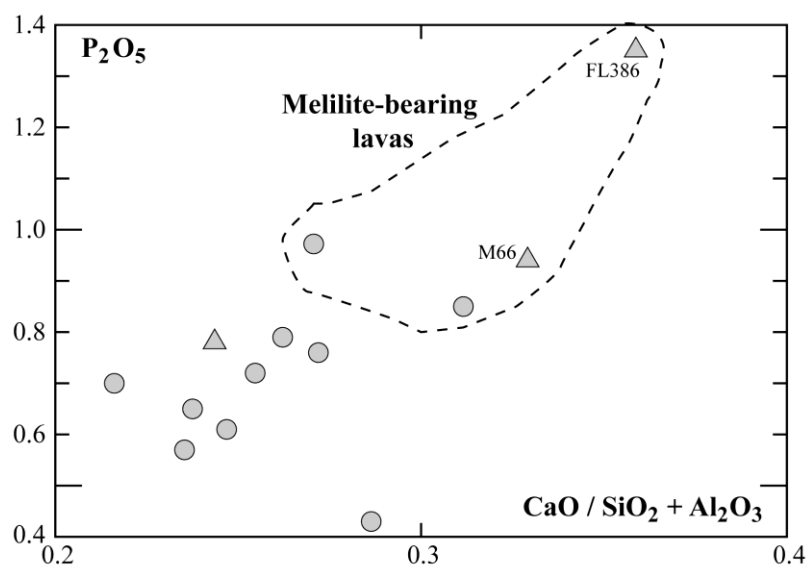
866 Fig. 7



867

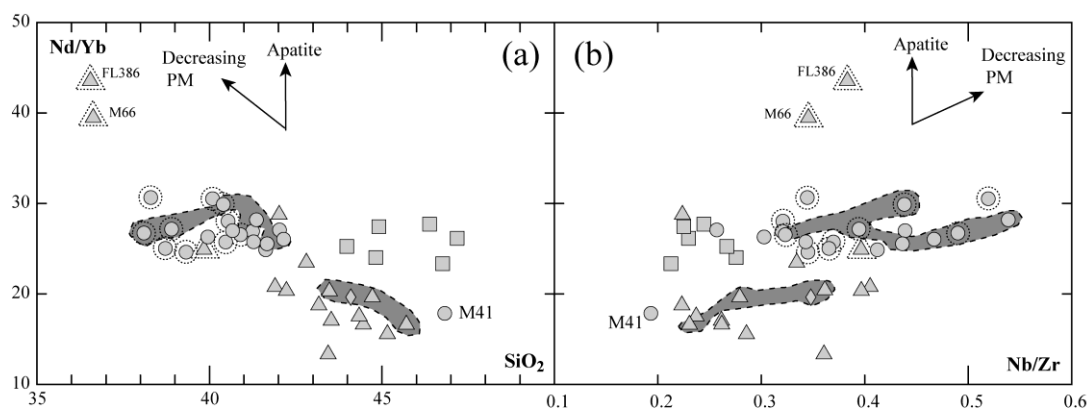
868 Fig. 8

869



870

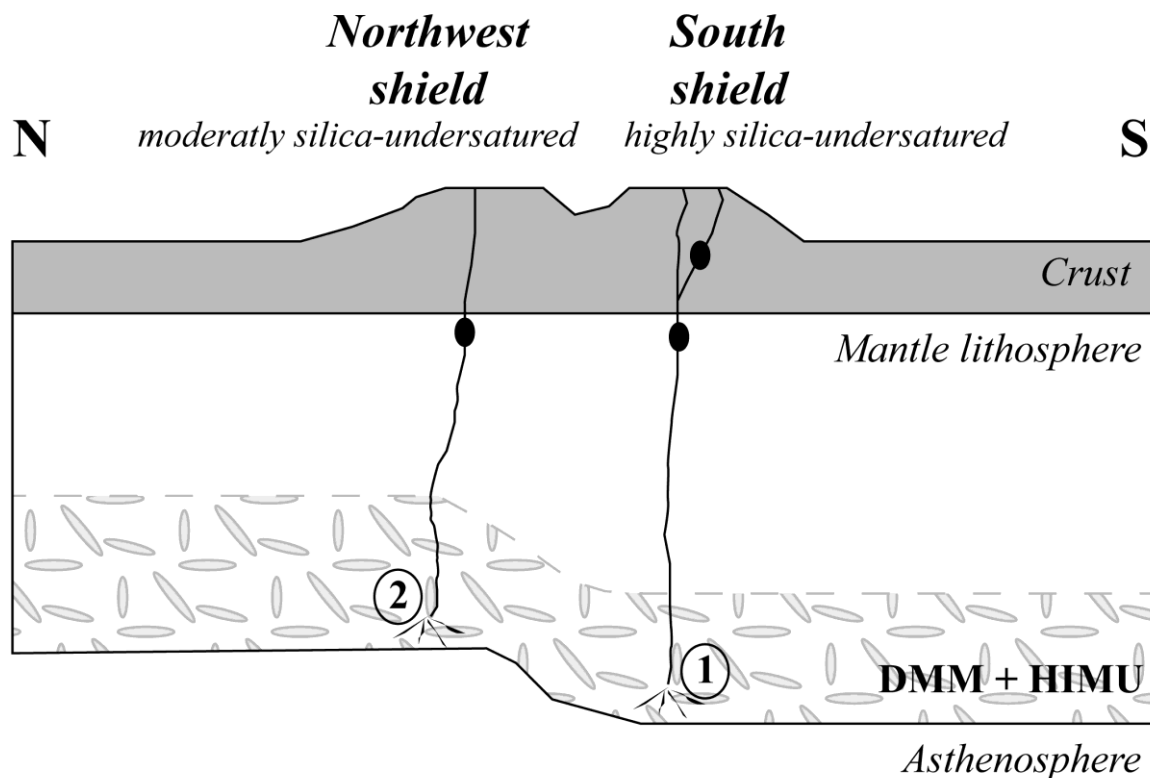
871 Fig. 9



872

873 Fig. 10

# Mayotte main building phase (> 10.6 - ~3.0 Ma)



874

875 Fig. 11

Table 1. Dating results from  $^{40}\text{Ar}$ - $^{39}\text{Ar}$  geochronology for Mayotte samples

Sample				Plateau age			Inverse isochron age					Integrated age	Preferred age	Remark
Unit	Number	Location	Petrological type	Type	Age (Ma)	Steps	Type	Age (Ma)	$^{40}\text{Ar}/^{36}\text{Ar}_i$	MSWD	Steps	Age (Ma)	Age (Ma)	
Northwest	M104	Lava flow	Basanite	SMA	$6.1 \pm 0.3$	1-3		$4.3 \pm 0.1$	$311 \pm 10$	0,1	1-6	$5.0 \pm 0.1$	$6.1 \pm 0.3$	SMA is maximum age Data too clustered on isochron
	M112	Dyke	Ol.-nephelinite	SMA	$5.2 \pm 0.3$	1-3		$4.4 \pm 1.0$	$305 \pm 10$	2,4	1-5	$5.3 \pm 0.1$	$4.4 \pm 1.0$	
	M108	Dyke in M104	Basanite	SMA	$3.8 \pm 0.1$	1-4		$4.2 \pm 0.8$	$291 \pm 10$	7,1	1-6, 8	$3.2 \pm 0.1$	$3.8 \pm 0.1$	
	M25	Lava flow	Alkali basalt	NO	-	-		$2.0 \pm 0.9$	$382 \pm 46$	26,8	1-4	$3.2 \pm 0.1$	$2.0 \pm 0.9$	Maximum age
	M20	Dyke	Basanite	SMA	$0.6 \pm 1.25$	4-5	NO	-	-	-	-	$8.9 \pm 0.2$	< 1 Ma	Maximum age
M59	Lava flow	Basanite	WMP	$0.8 \pm 0.2$	1-5		$0.8 \pm 0.1$	$303 \pm 150$	0,1	1-6	$0.8 \pm 0.2$	$0.8 \pm 0.2$	Data too clustered on isochron	
North central	M97	Lava flow	Basanite	SMA	$1.9 \pm 0.1$	1-5		$2.4 \pm 0.3$	$291 \pm 6$	4,8	1-5	$1.8 \pm 0.1$	$2.4 \pm 0.3$	
	M4	Lava flow	Tephrite	NO	-	-		$2.3 \pm 0.3$	$240 \pm 30$	12,7	1-3, 5-7	$3.5 \pm 0.6$	$2.3 \pm 0.3$	Maximum age
	M29	Dome	Trachyte	NO	-	-	NO	-	-	-	-	$2.9 \pm 0.6$	< 3 Ma	Maximum age
	M123	Lava flow	Tephriphonolite		$1.2 \pm 0.1$ /	-	NO	-	-	-	-	$1.2 \pm 0.1$ / $1.4 \pm 0.1$	$1.4 \pm 0.1$	
	M56	Lava flow	Basaltic trachy-andesite	SMA	$1.5 \pm 0.6$	1-3		$1.4 \pm 0.1$	$311 \pm 11$	2,6	1-4	$1.4 \pm 0.1$	$1.4 \pm 0.1$	
	M82	Lava flow	Basanite	SMA	$1.4 \pm 0.1$	1-4		$2.1 \pm 0.1$	$265 \pm 10$	0,9	1-4	$1.1 \pm 0.1$	$1.1 \pm 0.1$	
M58	Lava flow	Phonolite	SMA	$0.2 \pm 0.1$	1-3		$0.8 \pm 0.1$	$345 \pm 18$	4,3	1-6	$0.6 \pm 0.1$	$0.8 \pm 0.1$	Nice isochron	
Petite Terre	M53	Strombolian cone	Alkali basalt	NO	-	-	NO	-	-	-	-	$0.5 \pm 0.1$	$0.2 \pm 0.1$	All individual steps below 0.2 Ma
South	M137	Lava flow	Ol.-nephelinite	NO	-	-		$5.0 \pm 0.3$	$319 \pm 2$	1,1	1-6	$13.1 \pm 0.2$	$5.0 \pm 0.3$	
	M41	Lava flow	Alkali basalt	NO	-	-		$10.6 \pm 0.5$	$270 \pm 20$	5,9	2-6	$6.2 \pm 0.1$	$10.6 \pm 0.5$	Steps used are the richest in $^{39}\text{Ar}$
	M140	Lava flow	Ol.-free neph.	WMP	$5.9 \pm 0.1$	1-4		$6.1 \pm 0.1$	$306 \pm 5$	2,2	1-5	$5.8 \pm 0.1$	$5.9 \pm 0.1$	
	M93	Lava flow	Ol.-nephelinite	NO	-	-		$3.4 \pm 0.2$	$308 \pm 6$	4,8	1-4	$4.4 \pm 0.1$	$3.4 \pm 0.2$	
	M132	Lava flow	Ol.-nephelinite	SMA	$3.8 \pm 0.1$	2-4		$4.0 \pm 0.3$	$302 \pm 7$	5,5	1-6	$4.7 \pm 0.1$	$4.0 \pm 0.3$	
	M38	Lava flow	Ol.-nephelinite	SMA	$4.6 \pm 0.1$	1-2	NO	-	-	-	-	$3.9 \pm 0.1$	$3.9 \pm 0.1$	The integrated age is preferred to badly defined plateau
	M39A	Dome	Phonolite	WMP	$3.9 \pm 0.4$	2-7		$4.7 \pm 0.9$	$263 \pm 49$	0,8	2-7	$4.3 \pm 0.1$	$3.9 \pm 0.4$	Good plateau
	M55	Lava flow	Ol.-free neph.	NO	-	-		$3.6 \pm 0.4$	$291 \pm 42$	5,9	1-4, 7	$3.8 \pm 0.5$	$3.6 \pm 0.4$	
	M115	Lava flow	Ol.-nephelinite	NO	-	-		$1.9 \pm 0.2$	$327 \pm 11$	6,4	1-7	$2.1 \pm 0.4$	$1.9 \pm 0.2$	
M95	Lava flow	Ol.-nephelinite	SMA	$2.5 \pm 0.2$	1-2	NO	-	-	-	-	$1.5 \pm 0.8$	< 2.5 Ma		

For each sample, the plateau age and the isochron age are given when available; the preferred age is indicated in the last column.

MSWD: mean square weighted deviation. SMA: simple mean age, WMP: weighed plateau age.

Type of statistical approach: NO: no plateau or isochron could be calculated; SMA: simple mean age; WMP: weighed mean plateau age



**Table 2.** Major and trace elements data for Mayotte

Sample	Phonolitic pumices			Alkali basalts			Basanites					Olivine melilitites			
	M54 <sup>(1)</sup>	PN5a <sup>(2)</sup>	PN15 <sup>(2)</sup>	M25 <sup>(1)</sup>	M41 <sup>(1)</sup>	M75 <sup>(1)</sup>	M35 <sup>(1)</sup>	M60 <sup>(1)</sup>	M82 <sup>(1)</sup>	M97 <sup>(1)</sup>	M108 <sup>(1)</sup>	PN3 <sup>(2)</sup>	PN5b <sup>(2)</sup>	FL386 <sup>(2)</sup>	M66 <sup>(1)</sup>
Location	PT	PT	PT	NW	S	NC	S	NW	NC	NC	NW	S	PT	NW	NW
<b>Major elements (wt. %)</b>															
SiO <sub>2</sub>	58.42	57.80	57.70	45.71	46.82	47.18	42.03	42.02	44.91	43.98	44.72	41.67	44.08	36.55	36.63
TiO <sub>2</sub>	-	0.07	0.06	2.28	2.75	2.74	3.45	3.14	3.28	2.77	2.26	2.36	1.91	3.01	2.44
Al <sub>2</sub> O <sub>3</sub>	19.21	18.30	18.30	12.20	13.79	15.32	11.60	11.70	15.74	12.55	11.46	11.50	10.11	9.64	9.49
Fe <sub>2</sub> O <sub>3</sub> (total)	5.82	5.80	5.80	13.52	12.80	12.81	13.86	14.03	12.57	13.84	13.03	12.42	10.42	14.29	13.25
MnO	0.25	0.24	0.25	0.18	0.16	0.17	0.16	0.17	0.18	0.20	0.19	0.22	0.15	0.23	0.21
MgO	0.13	0.14	0.24	10.93	7.09	5.85	10.84	12.22	5.49	10.66	11.12	12.80	10.86	13.44	14.63
CaO	1.20	1.21	1.17	11.24	11.35	8.84	11.74	10.53	9.18	10.97	11.83	12.46	15.46	16.57	15.18
Na <sub>2</sub> O	8.24	7.80	7.99	2.70	2.61	3.09	2.98	2.35	3.50	2.84	3.02	2.88	1.78	2.50	3.36
K <sub>2</sub> O	5.55	5.38	5.20	0.99	1.06	1.91	0.45	1.42	1.89	1.36	1.12	0.59	0.79	0.62	1.18
P <sub>2</sub> O <sub>5</sub>	0.13	0.09	0.10	0.37	0.39	0.64	0.50	0.55	0.71	0.55	0.42	0.60	0.32	1.35	0.94
LOI	0.93	2.54	3.29	-0.15	1.10	1.45	2.39	1.08	2.54	0.18	0.73	3.40	3.78	2.95	1.63
Total	99.88	99.31	100.10	99.97	99.92	100.00	100.00	99.21	99.99	99.90	99.90	100.88	98.38	101.15	98.94
<sub>N</sub> Larnite	-	-	-	-	-	-	-	-	-	-	-	-	-	11.80	14.38
<sub>N</sub> Nepheline	-	-	-	5.13	0.31	0.59	8.93	8.02	5.76	8.42	9.61	12.13	6.87	11.46	15.40
<b>Trace elements (ppm)</b>															
Li	-	23.7	24.5	-	-	-	-	-	-	-	-	7.6	9.6	11.4	-
Be	5.9	5.8	5.6	1.5	-	-	2.0	-	2.1	-	-	1.8	1.2	2.4	1.7
Rb	162	163	149	22	23	43	62	38	50	33	30	20	21	20	32
Sr	26.1	32.6	25.0	530	495	913	761	609	980	948	494	828	419	2087	1083
Ba	114	136	121	316	327	707	563	546	652	546	407	648	238	719	674
Cs	1.28	1.55	1.41	0.25	-	0.44	0.58	0.52	0.51	0.27	0.26	0.54	0.36	0.40	0.43
V	-	-	-	265	290	205	322	242	219	253	258	279	258	255	246
Cr	-	-	-	787	149	145	563	380	58	402	714	626	472	465	626
Ni	-	-	-	263	116	119	277	364	48	265	238	357	168	270	365
Co	-	-	-	62	49	40	65	71	35	62	59	66	45	64	65
Sc	-	13	12	-	-	-	-	-	-	-	-	28	51	25	-
Cu	-	10	6.5	89	114	45	81	62	40	70	100	75	74	73	67
Zn	207	185	162	132	126	159	124	140	141	138	111	109	74	137	124
Y	46	46	44	24	25	28	22	22	27	24	21	27	21	34	29
Zr	1141	1262	1195	173	222	325	208	218	303	225	156	215	145	350	270
Nb	292	336	316	40	43	75	53	49	68	59	44	94	50	134	93
Hf	24	24	23	4.1	5.3	7.1	5.2	5.2	6.7	5.4	4.2	4.8	3.5	7.3	5.5
Ta	18	17	16	3.0	3.0	5.0	4.0	4.0	5.0	4.0	3.5	5.0	2.5	7.0	6.0
La	151.2	171.3	166.2	30.9	37.5	55.6	42.7	43.2	50.3	45.8	36.1	58.9	35.6	102.9	89.5
Ce	282.6	291.0	281.9	64.9	76.7	112.8	85.9	91.3	108.5	90.9	74.5	113.9	66.5	204.6	163.2
Pr	28.7	26.8	25.6	7.20	8.85	12.9	10.1	10.4	12.9	10.5	8.50	12.6	7.43	22.4	19.5
Nd	88.2	85.5	83.6	30.0	36.6	48.9	39.8	41.7	50.2	42.4	32.6	47.8	29.6	88.0	74.2
Sm	13.5	13.6	13.2	6.46	7.56	9.59	8.41	8.35	9.66	7.81	6.46	9.14	5.66	16.5	13.3
Eu	1.63	1.65	1.60	2.09	2.45	3.12	2.62	2.67	3.11	2.64	2.15	2.73	1.81	4.68	4.02
Gd	9.55	10.5	10.5	6.05	6.80	8.05	7.00	7.15	8.10	6.90	5.90	8.55	5.40	14.0	10.0
Tb	1.60	1.65	1.65	0.80	0.90	1.05	0.90	0.95	1.15	0.95	0.80	1.15	0.75	1.75	1.35
Dy	8.91	9.24	8.84	4.60	5.00	5.79	4.68	5.06	5.90	5.15	4.45	5.69	4.07	7.81	6.60
Ho	1.66	1.78	1.75	0.79	0.86	0.97	0.78	0.81	0.99	0.87	0.76	1.02	0.75	1.29	1.05
Er	4.73	5.13	5.04	2.04	2.24	2.53	1.80	1.97	2.37	2.15	1.99	2.56	1.87	3.03	2.53
Yb	4.92	5.24	5.08	1.81	2.05	1.87	1.47	1.45	1.83	1.68	1.66	1.87	1.51	2.02	1.88
Lu	0.79	0.76	0.75	0.26	0.28	0.28	0.19	0.21	0.27	0.21	0.24	0.25	0.21	0.26	0.27
Th	22.6	21.3	21.4	3.7	4.3	7.8	5.7	5.2	6.4	5.3	4.7	6.8	3.9	12.0	9.8
U	5.8	5.8	5.7	0.9	1.0	1.8	1.3	1.4	1.7	1.4	1.0	1.5	0.8	3.2	2.8
Pb	11.3	19.3	8.9	2.9	2.8	4.6	3.1	2.6	3.8	2.9	3.5	4.7	5.2	5.1	2.7

		Olivine nephelinites													
Sample	FL468 <sup>(2)</sup>	J2 <sup>(2)</sup>	M19 <sup>(1)</sup>	M50 <sup>(1)</sup>	M88 <sup>(1)</sup>	M89 <sup>(1)</sup>	M112 <sup>(1)</sup>	M129 <sup>(1)</sup>	M132 <sup>(1)</sup>	M133 <sup>(1)</sup>	M135 <sup>(1)</sup>	M137 <sup>(1)</sup>	M138 <sup>(1)</sup>	PN2 <sup>(2)</sup>	PN12 <sup>(2)</sup>
Location	S	S	NW	S	S	S	NW	S	S	S	S	S	S	S	S
<b>Major elements (wt. %)</b>															
SiO <sub>2</sub>	41.36	42.15	39.84	40.09	39.32	40.47	43.44	38.30	40.90	40.40	41.28	40.54	38.72	38.90	38.10
TiO <sub>2</sub>	2.31	2.52	3.07	2.65	3.41	3.26	2.17	3.51	2.83	2.36	2.98	2.41	2.84	3.10	2.56
Al <sub>2</sub> O <sub>3</sub>	15.62	12.93	13.98	14.10	13.48	15.15	12.27	11.65	15.50	13.00	13.42	11.35	14.07	11.23	12.00
Fe <sub>2</sub> O <sub>3</sub> (total)	12.98	12.45	14.43	12.81	12.58	12.77	12.91	12.86	12.06	11.74	12.52	12.20	12.56	13.67	12.70
MnO	0.28	0.23	0.23	0.23	0.16	0.19	0.20	0.18	0.21	0.24	0.20	0.21	0.23	0.22	0.24
MgO	6.11	7.85	6.71	6.69	8.23	6.70	10.68	9.97	6.01	8.90	8.33	13.88	6.68	10.21	10.30
CaO	11.27	14.67	13.11	13.80	15.12	13.09	12.60	12.33	12.19	14.00	12.47	14.11	12.54	15.62	13.56
Na <sub>2</sub> O	5.11	3.71	4.06	3.82	3.80	4.60	3.26	4.22	4.41	5.17	4.30	2.48	5.51	3.10	3.56
K <sub>2</sub> O	1.70	0.91	1.48	1.18	0.80	1.07	1.45	0.86	2.61	2.32	1.04	1.18	1.76	0.81	0.93
P <sub>2</sub> O <sub>5</sub>	1.06	0.68	0.78	0.72	0.43	0.57	0.48	0.61	0.70	0.79	0.64	0.76	0.65	0.85	0.97
LOI	2.73	2.84	2.20	3.93	2.63	2.13	0.66	4.02	2.63	0.72	2.45	0.59	3.49	2.59	4.55
Total	100.54	100.93	99.89	100.02	99.96	100.00	100.12	98.51	100.05	99.64	99.63	99.62	99.05	100.31	99.47
<sub>N</sub> Larnite	-	-	1.52	1.03	5.65	0.68	-	2.37	1.49	8.92	-	4.58	5.47	6.53	4.22
<sub>N</sub> Nepheline	23.42	17.01	18.61	17.51	17.42	21.09	14.94	19.34	20.22	23.70	19.71	11.37	25.26	14.21	16.32
<b>Trace elements (ppm)</b>															
Li	13.3	10.5	-	-	-	-	-	-	-	-	-	-	-	10.3	16.0
Be	3.5	2.8	3.0	2.6	1.5	2.0	-	-	2.8	2.1	2.1	-	2.6	2.3	2.6
Rb	45	30	42	22	11	14	45	28	58	65	17	28	48	27	27
Sr	1528	878	843	1064	727	873	645	757	1143	1297	815	746	1072	1154	1368
Ba	946	858	920	875	587	829	568	587	849	1069	721	572	867	743	960
Cs	0.80	2.65	1.05	0.65	0.36	0.54	0.62	0.36	0.68	0.65	0.78	0.24	1.20	0.55	0.20
V	252	320	324	307	372	305	274	304	241	221	311	212	306	330	286
Cr	62	183	76	110	180	77	581	451	109	315	507	547	182	337	332
Ni	46	98	53	55	69	41	200	193	61	143	160	300	86	181	165
Co	43	59	48	42	46	39	57	54	36	41	50	78	46	60	54
Se	16	32	-	-	-	-	-	-	-	-	-	-	-	30	23
Cu	65	150	73	83	88	37	105	83	55	67	94	65	85	102	77
Zn	145	118	143	124	96	113	117	107	135	116	128	118	135	123	124
Y	40	31	31	29	24	27	24	23	31	37	29	24	29	32	33
Zr	324	246	262	235	170	239	185	205	299	261	251	230	271	282	266
Nb	175	115	104	122	59	89	67	70	97	115	86	74	99	111	131
Hf	5.7	5.1	5.7	5.0	5.2	5.6	4.0	4.7	5.9	5.1	5.3	4.6	5.5	6.1	5.4
Ta	9.0	5.0	7.0	6.5	4.5	6.5	4.5	5.0	7.5	7.5	6.5	5.0	6.5	5.5	7.0
La	118.8	76.0	83.6	91.2	47.7	65.0	53.9	50.1	78.0	134.7	65.1	84.2	73.9	74.3	92.0
Ce	221.6	140.6	151.9	168.0	99.6	129.1	98.2	99.4	145.7	218.9	125.4	120.1	136.0	140.0	168.3
Pr	23.0	15.1	16.4	17.6	11.2	14.1	10.4	11.8	16.1	23.5	14.2	13.1	14.9	15.5	17.9
Nd	81.8	56.5	59.2	65.6	45.3	53.5	38.8	46.6	62.1	81.9	54.9	49.1	56.0	59.7	67.1
Sm	14.1	10.3	10.2	10.9	8.23	9.49	7.11	8.83	10.9	13.1	10.0	8.50	9.93	11.5	11.9
Eu	3.98	3.01	3.18	3.31	2.55	2.92	2.21	2.71	3.38	3.89	3.12	2.67	3.06	3.38	3.49
Gd	12.5	9.50	8.75	8.90	7.10	7.75	6.00	7.15	8.90	10.0	8.25	7.05	8.20	10.5	10.5
Tb	1.65	1.25	1.20	1.20	0.95	1.05	0.85	0.95	1.25	1.40	1.15	0.95	1.15	1.35	1.40
Dy	7.74	6.13	6.38	6.05	5.00	5.68	4.65	4.96	6.40	7.35	6.04	5.08	6.08	6.79	7.05
Ho	1.44	1.13	1.12	1.04	0.90	0.99	0.82	0.83	1.16	1.28	1.02	0.81	1.06	1.20	1.28
Er	3.65	2.86	2.96	2.70	2.27	2.55	2.06	1.98	2.88	3.36	2.59	2.16	2.65	2.97	3.25
Yb	2.90	2.17	2.38	2.15	1.84	2.08	1.91	1.52	2.34	2.74	2.13	1.75	2.24	2.20	2.51
Lu	0.40	0.29	0.35	0.31	0.27	0.31	0.27	0.21	0.33	0.39	0.30	0.25	0.33	0.29	0.34
Th	13.0	9.6	10.6	9.1	6.6	8.8	7.1	5.4	10.0	13.5	7.2	9.1	8.0	8.4	10.4
U	5.1	2.2	2.3	2.2	1.6	2.0	1.6	1.3	2.6	3.2	1.5	2.0	1.9	2.1	3.1
Pb	7.4	5.8	6.0	5.3	3.3	4.2	4.7	7.6	6.2	7.9	4.3	4.7	11.0	5.0	6.4

Sample	Olivine-free nephelinites		Tephrites		Tephri-phonolites				Phonolites						
	M140 <sup>(1)</sup>	PN8 <sup>(2)</sup>	J7 <sup>(2)</sup>	M4 <sup>(1)</sup>	FL478 <sup>(2)</sup>	M91 <sup>(1)</sup>	M123 <sup>(1)</sup>	M127 <sup>(1)</sup>	FL426 <sup>(2)</sup>	FL442 <sup>(2)</sup>	M58 <sup>(1)</sup>	M103 <sup>(1)</sup>	M131 <sup>(1)</sup>	PN7 <sup>(2)</sup>	PN11 <sup>(2)</sup>
Location	S	S	NC	NC	S <sup>C</sup>	S	NC	NW	S <sup>C</sup>	S <sup>C</sup>	NC	S <sup>C</sup>	S	S	NC
<b>Major elements (wt. %)</b>															
SiO <sub>2</sub>	47.15	46.02	49.02	46.38	49.94	50.24	55.00	51.66	53.55	54.58	58.98	54.34	54.47	53.91	55.85
TiO <sub>2</sub>	1.09	1.26	2.46	2.94	1.70	0.67	1.22	1.03	0.48	0.49	0.33	0.71	0.25	0.31	0.30
Al <sub>2</sub> O <sub>3</sub>	20.41	18.82	16.16	15.18	17.70	19.96	19.43	18.22	19.31	20.48	20.00	20.16	20.39	19.07	21.42
Fe <sub>2</sub> O <sub>3</sub> (total)	7.89	7.88	10.91	12.42	9.42	6.54	6.21	8.31	5.80	4.78	3.49	5.62	4.37	5.67	2.75
MnO	0.22	0.29	0.18	0.17	0.25	0.27	0.14	0.28	0.27	0.19	0.14	0.19	0.22	0.29	0.17
MgO	1.85	1.97	4.26	5.50	2.40	0.90	1.53	0.73	0.78	0.90	0.21	1.35	0.41	0.33	0.24
CaO	6.85	6.15	7.28	9.08	5.13	4.17	4.19	3.73	2.34	1.65	1.32	2.51	1.54	1.29	1.30
Na <sub>2</sub> O	6.79	8.25	4.82	4.27	7.38	7.25	6.60	8.07	8.24	9.37	8.03	8.95	8.77	8.29	9.61
K <sub>2</sub> O	4.17	4.46	2.67	2.08	4.42	5.69	4.21	5.43	4.57	5.25	5.70	4.98	5.37	6.35	5.72
P <sub>2</sub> O <sub>5</sub>	0.35	0.31	0.74	0.62	0.65	0.17	0.39	0.32	0.17	0.15	0.05	0.27	0.05	0.02	0.03
LOI	3.32	4.13	0.59	1.35	1.26	4.25	1.11	2.61	3.12	1.22	1.65	1.02	4.09	3.78	1.32
Total	100.09	99.15	99.09	98.64	100.25	100.11	100.03	100.39	98.63	99.07	99.90	100.10	99.93	98.75	98.71
<sub>N</sub> Larnite	-	-	-	-	-	-	-	-	-	-	-	-	-	-	-
<sub>N</sub> Nepheline	-	-	-	-	-	-	-	-	-	-	-	-	-	-	-
<b>Trace elements (ppm)</b>															
Li	-	21.5	14.0	-	13.4	-	-	-	7.1	14.4	-	-	-	2.6	17.6
Be	4.5	7.3	3.5	2.5	3.3	7.5	3.4	4.3	6.7	4.2	8.2	2.1	8.7	10.7	6.9
Rb	131	146	78.1	30.7	146	214	104	174	230	172	187	150	162	242	202
Sr	1341	1828	1091	964	1916	1284	1040	1428	668	1439	213	1520	764	1035	268
Ba	1262	2064	856	788	1350	1380	1084	1765	506	811	561	1032	277	764	206
Cs	1.28	1.21	1.08	1.24	1.29	1.95	1.34	0.83	2.09	1.43	1.90	2.30	2.13	1.32	2.58
V	64	107	177	224	103	53	54	15.7	10.8	11	2.8	31	9.2	9.1	15
Cr	-	3.5	59	153	12	-	-	-	1.2	11	-	19	-	-	0.4
Ni	-	3.0	55	90	15	-	5.5	-	1.7	12	-	18	-	-	0.5
Co	12	12	35	44	16	5.5	10	5.2	2.3	3.2	1.2	5.8	1.0	1.4	1.4
Sc	-	2.0	14	-	5.4	-	-	-	1.6	1.4	-	-	-	0.9	1.1
Cu	16	12	41	53	15	4.8	11	-	0.7	1.9	-	5.9	-	0.5	1.2
Zn	156	179	154	155	146	194	135	172	189	132	144	128	175	246	137
Y	33	53	31	27	47	38	25	41	36	27	24	28	32	55	19
Zr	340	596	529	350	668	594	640	790	1067	846	879	731	701	862	953
Nb	145	240	126	86	233	182	113	159	317	257	132	175	151	298	164
Hf	6.0	7.5	9.3	8.2	11.4	7.9	11.2	12.5	18.2	15.4	14.1	13.1	8.7	10.2	13.4
Ta	9.0	8.0	6.0	6.0	13	5.0	9.5	14	18	17	10	16	6.0	5.0	4.5
La	116.1	154.4	74.4	65.2	127.0	97.2	79.3	113.7	66.0	65.3	98.7	78.4	85.8	102.9	81.7
Ce	191.6	243.2	138.2	125.8	224.1	142.8	145.4	203.0	126.6	123.1	138.3	141.9	140.8	168.4	106.0
Pr	19.5	22.1	15.0	13.8	22.9	14.6	15.2	23.3	13.6	12.8	12.0	15.3	12.5	14.8	7.99
Nd	64.4	73.2	55.6	52.4	80.2	45.8	48.2	83.5	47.9	44.9	35.3	54.3	38.7	45.2	21.2
Sm	9.94	11.9	10.5	9.72	14.0	7.37	7.16	13.8	8.98	7.93	4.83	8.81	6.14	7.60	2.83
Eu	3.16	3.53	3.19	3.14	4.21	2.33	2.51	4.13	2.66	2.50	1.22	2.92	1.91	2.41	0.78
Gd	7.80	10.5	9.40	3.75	12.0	6.40	5.95	10.0	8.15	6.90	3.35	6.50	4.80	7.65	2.45
Tb	1.15	1.50	1.30	1.05	1.65	1.00	0.85	1.50	1.20	1.00	0.55	0.95	0.80	1.30	0.40
Dy	6.48	8.35	6.28	5.90	8.41	6.23	4.59	8.43	6.74	5.25	3.65	5.37	5.60	7.78	2.44
Ho	1.17	1.64	1.14	0.89	1.58	1.23	0.82	1.42	1.32	1.02	0.71	0.85	1.06	1.64	0.56
Er	3.22	4.67	2.79	2.39	4.19	3.72	2.31	3.96	3.86	2.84	1.97	2.50	3.21	5.25	1.87
Yb	3.04	4.02	2.21	1.89	3.40	3.92	1.95	4.13	3.84	2.65	2.47	2.60	3.41	5.19	2.31
Lu	0.45	0.53	0.29	0.29	0.47	0.57	0.31	0.60	0.54	0.38	0.35	0.39	0.50	0.71	0.34
Th	22.3	30.1	11.5	9.6	15.7	25.5	19.5	20.0	24.6	12.9	24.8	12.7	27.7	34.1	24.1
U	5.0	5.1	3.2	2.6	5.4	7.6	4.9	4.6	6.7	3.5	3.9	4.3	7.4	10.3	8.4
Pb	12.7	23.4	5.9	5.0	5.3	20.8	9.6	11.4	12.3	7.5	16.2	7.2	17.9	26.3	11.2

S: south domain; S<sup>C</sup>: Comban; NW: northwest domain; NC: north central domain; PT: Petite Terre. <sub>N</sub>Larnite for normative larnite; <sub>N</sub>Nepheline for normative nepheline. CIPW norms was calculated for basic lavas using the ratio: Fe<sub>2</sub>O<sub>3</sub>/Fe<sub>2</sub>O<sub>3(total)</sub>=0.15. (1) Samples collected in 2001, major and trace elements analyzed by ICP-AES and ICP-MS respectively (CRPG, Nancy, France). (2) Samples collected during two field trips in 2010 and 2011, major elements analyzed by ICP-AES (PSO/IUEM, Brest, France) following the analytical method described by Cotten et al (1995), trace elements analyzed by ICP-MS (PSO/IUEM, Brest, France) following the sample preparation and analysis method of Barrat et al (1996).

Table 3. Sr, Nd, Pb isotopic data for Mayotte.

(1) S: south domain; S<sup>C</sup>: Combani Massif; NW: northwest domain; NC: north central domain; PT: Petite Terre domain (see Fig. 2c for domain location).(2) Sr and Nd isotopic ratios measured in 2003 on a TI-MS (Laboratoire Magmas et Volcans, Clermont-Ferrand, France) – Debeuf (2004). Average value of NBS 987 (standard for Sr) is  $^{87}\text{Sr}/^{86}\text{Sr} = 0.710253 \pm 0.000020$ 

Sample	Rock Type	Location <sup>(1)</sup>	$^{87}\text{Sr}/^{86}\text{Sr}$	2 $\sigma$	$^{143}\text{Nd}/^{144}\text{Nd}$	2 $\sigma$	$^{206}\text{Pb}/^{204}\text{Pb}$	2 $\sigma$	$^{207}\text{Pb}/^{204}\text{Pb}$	2 $\sigma$	$^{208}\text{Pb}/^{204}\text{Pb}$	2 $\sigma$
PN5a	Phon. pumice	PT	-	-	0.512856 <sup>(4)</sup>	0.000008	19.4841 <sup>(4)</sup>	0.0006	15.6263 <sup>(4)</sup>	0.0006	39.377 <sup>(4)</sup>	0.002
M25	Alkali basalt	NW	0.703350 <sup>(2)</sup>	0.000006	0.512860 <sup>(4)</sup>	0.000004	20.2819 <sup>(4)</sup>	0.0006	15.6699 <sup>(4)</sup>	0.0007	39.965 <sup>(4)</sup>	0.002
M41	Alkali basalt	S	0.703830 <sup>(2)</sup>	0.000006	0.512720 <sup>(2)</sup>	0.000004	-	-	-	-	-	-
M60	Basanite	NW	0.703300 <sup>(2)</sup>	0.000006	0.512860 <sup>(2)</sup>	0.000004	-	-	-	-	-	-
M82	Basanite	NC	-	-	0.512860 <sup>(2)</sup>	0.000004	-	-	-	-	-	-
M97	Basanite	NC	0.703350 <sup>(2)</sup>	0.000006	0.512880 <sup>(2)</sup>	0.000004	19.1269 <sup>(4)</sup>	0.0006	15.5746 <sup>(4)</sup>	0.0006	39.059 <sup>(4)</sup>	0.002
M108	Basanite	NW	0.703390 <sup>(2)</sup>	0.000006	0.512820 <sup>(2)</sup>	0.000004	20.3206 <sup>(4)</sup>	0.0008	15.6738 <sup>(4)</sup>	0.0007	40.028 <sup>(4)</sup>	0.002
PN3	Basanite	S	0.703241 <sup>(3)</sup>	0.000006	0.512862 <sup>(3)</sup>	0.000010	20.1820 <sup>(3)</sup>	0.0010	15.6641 <sup>(3)</sup>	0.0009	39.929 <sup>(3)</sup>	0.003
PN5b	Basanite	PT	-	-	0.512784 <sup>(4)</sup>	0.000004	19.8709 <sup>(4)</sup>	0.0009	15.6698 <sup>(4)</sup>	0.0008	39.718 <sup>(4)</sup>	0.003
FL386	Ol.-melilitite	NW	0.703254 <sup>(3)</sup>	0.000006	0.512860 <sup>(3)</sup>	0.000008	19.4139 <sup>(3)</sup>	0.0007	15.6150 <sup>(3)</sup>	0.0007	39.282 <sup>(3)</sup>	0.002
M66	Ol.-melilitite	NW	-	-	0.512864 <sup>(4)</sup>	0.000003	19.5269 <sup>(4)</sup>	0.0006	15.6238 <sup>(4)</sup>	0.0006	39.379 <sup>(4)</sup>	0.002
FL468	Ol.-nephelinite	S	0.703307 <sup>(3)</sup>	0.000006	0.512823 <sup>(3)</sup>	0.000004	20.1553 <sup>(3)</sup>	0.0008	15.6589 <sup>(3)</sup>	0.0007	39.883 <sup>(3)</sup>	0.002
J2	Ol.-nephelinite	S	0.703418 <sup>(3)</sup>	0.000008	0.512795 <sup>(3)</sup>	0.000006	20.1919 <sup>(3)</sup>	0.0006	15.6664 <sup>(3)</sup>	0.0006	39.930 <sup>(3)</sup>	0.002
M112	Ol.-nephelinite	NW	0.703380 <sup>(2)</sup>	0.000006	0.512820 <sup>(2)</sup>	0.000004	20.2677 <sup>(4)</sup>	0.0006	15.6606 <sup>(4)</sup>	0.0008	39.961 <sup>(4)</sup>	0.003
M132	Ol.-nephelinite	S	0.703410 <sup>(2)</sup>	0.000006	0.512860 <sup>(2)</sup>	0.000004	20.2718 <sup>(4)</sup>	0.0007	15.6700 <sup>(4)</sup>	0.0006	39.993 <sup>(4)</sup>	0.002
M133	Ol.-nephelinite	S	-	-	0.512820 <sup>(4)</sup>	0.000004	20.0849 <sup>(4)</sup>	0.0005	15.6608 <sup>(4)</sup>	0.0005	39.856 <sup>(4)</sup>	0.001
M137	Ol.-nephelinite	S	0.703320 <sup>(2)</sup>	0.000006	0.512860 <sup>(2)</sup>	0.000004	19.5055 <sup>(4)</sup>	0.0005	15.6096 <sup>(4)</sup>	0.0006	39.391 <sup>(4)</sup>	0.002
PN2	Ol.-nephelinite	S	0.703253 <sup>(3)</sup>	0.000006	0.512851 <sup>(3)</sup>	0.000004	20.0507 <sup>(3)</sup>	0.0009	15.6482 <sup>(3)</sup>	0.0009	39.799 <sup>(3)</sup>	0.003
PN12f	Ol.-nephelinite	S	-	-	0.512833 <sup>(4)</sup>	0.000004	20.3627 <sup>(4)</sup>	0.0007	15.6746 <sup>(4)</sup>	0.0007	40.091 <sup>(4)</sup>	0.002
M140	Ol.-free neph.	S	0.703410 <sup>(2)</sup>	0.000006	0.512800 <sup>(2)</sup>	0.000004	-	-	-	-	-	-
PN8	Ol.-free neph.	S	0.703269 <sup>(3)</sup>	0.000008	0.512858 <sup>(3)</sup>	0.000006	20.2067 <sup>(3)</sup>	0.0008	15.6645 <sup>(3)</sup>	0.0007	39.957 <sup>(3)</sup>	0.002
J7	Tephrite	NC	0.703333 <sup>(3)</sup>	0.000008	0.512891 <sup>(3)</sup>	0.000006	19.1695 <sup>(3)</sup>	0.0007	15.5792 <sup>(3)</sup>	0.0007	39.085 <sup>(3)</sup>	0.002
M56	Bas. trachy-and.	NC	0.703280 <sup>(3)</sup>	0.000006	0.512890 <sup>(2)</sup>	0.000004	-	-	-	-	-	-
FL426	Phonolite	S <sup>C</sup>	-	-	0.512848 <sup>(4)</sup>	0.000004	19.7492 <sup>(4)</sup>	0.0009	15.6219 <sup>(4)</sup>	0.0008	39.588 <sup>(4)</sup>	0.003
M123	Tephriphonolite	NC	0.703310 <sup>(2)</sup>	0.000006	0.512880 <sup>(2)</sup>	0.000004	-	-	-	-	-	-
FL442	Phonolite	S <sup>C</sup>	0.703198 <sup>(3)</sup>	0.000006	0.512871 <sup>(3)</sup>	0.000006	19.6438 <sup>(3)</sup>	0.0004	15.6084 <sup>(3)</sup>	0.0003	39.487 <sup>(3)</sup>	0.001
M58	Phonolite	NC	0.703410 <sup>(2)</sup>	0.000006	0.512870 <sup>(2)</sup>	0.000004	-	-	-	-	-	-
PN7	Phonolite	S	-	-	0.512834 <sup>(4)</sup>	0.000004	20.3548 <sup>(4)</sup>	0.0006	15.6775 <sup>(4)</sup>	0.0006	40.075 <sup>(4)</sup>	0.002
PN11	Phonolite	NC	0.703263 <sup>(3)</sup>	0.000006	0.512899 <sup>(3)</sup>	0.000004	19.3220 <sup>(3)</sup>	0.0007	15.5964 <sup>(3)</sup>	0.0007	39.215 <sup>(3)</sup>	0.002

(1 $\sigma$ ; n=39) and average value of Rennes-AMES (internal standard for Nd) is  $^{143}\text{Nd}/^{144}\text{Nd} = 0.511960 \pm 0.000010$  (1 $\sigma$ ; n=41).(3) Sr and Nd isotopic ratios measured in 2013 on a TI-MS (PSO/IUEM, Brest, France). Sr and Nd isotopic values are corrected for mass fractionation to  $^{88}\text{Sr}/^{86}\text{Sr} = 8.372509$  and  $^{146}\text{Nd}/^{144}\text{Nd} = 0.721903$  respectively. Average value of NBS 987 is  $^{87}\text{Sr}/^{86}\text{Sr} = 0.710237 \pm 0.000006$  (2 $\sigma$ ; n=8) and average value of La Jolla (standard for Nd) is  $^{143}\text{Nd}/^{144}\text{Nd} = 0.511873 \pm 0.000008$  (2 $\sigma$ ; n=6). Pb isotopic ratios measurements were performed by a MC-ICP-MS (PSO/IFREMER, Brest, France). Pb isotopic values are corrected for drift of  $^{205}\text{Tl}/^{203}\text{Tl}$  ratio and for the blank. Average values of NIST SRM 981 (standard for Pb) are  $^{206}\text{Pb}/^{204}\text{Pb} = 16.9314 \pm 0.0005$  (2 $\sigma$ ; n=7);  $^{207}\text{Pb}/^{204}\text{Pb} = 15.4850 \pm 0.0006$  (2 $\sigma$ ; n=7);  $^{208}\text{Pb}/^{204}\text{Pb} = 36.6764 \pm 0.0018$  (2 $\sigma$ ; n=7).(4) Nd and Pb isotopic ratios measured in february 2014 on a MC-ICP-MS (PSO/IFREMER, Brest, France). Nd isotopic values are corrected for mass fractionation to  $^{146}\text{Nd}/^{144}\text{Nd} = 0.721903$ . Average values of JNDi and La Jolla (standards for Nd) are  $^{143}\text{Nd}/^{144}\text{Nd} = 0.512105 \pm 0.000008$  (2 $\sigma$ ; n=6) and  $^{143}\text{Nd}/^{144}\text{Nd} = 0.511859 \pm 0.000010$  (2 $\sigma$ ; n=4) respectively. Pb isotopic values are corrected for drift of  $^{205}\text{Tl}/^{203}\text{Tl}$  ratio and for the blank. Average values of NIST SRM 981 (standard for Pb) are  $^{206}\text{Pb}/^{204}\text{Pb} = 16.9300 \pm 0.0006$  (2 $\sigma$ ; n=10);  $^{207}\text{Pb}/^{204}\text{Pb} = 15.4844 \pm 0.0007$  (2 $\sigma$ ; n=10);  $^{208}\text{Pb}/^{204}\text{Pb} = 36.6743 \pm 0.0019$  (2 $\sigma$ ; n=10).